

Metal enrichment in the circumgalactic medium and Ly α haloes around quasars at $z \sim 3$

YUCHENG GUO,^{1,2,3,4} ROBERTO MAIOLINO,^{3,4} LINHUA JIANG,¹ KENTA MATSUOKA,^{5,6} TOHRU NAGAO,⁷
OLI LUIZ DORS JUNIOR,⁸ MICHELE GINOLFI,⁹ NICK HENDEN,^{10,4} JAKE BENNETT,^{10,4} DEBORA SIJACKI,^{10,4} AND
EWALD PUCHWEIN¹¹

¹*Kavli Institute for Astronomy and Astrophysics, Peking University, Beijing 100871, China*

²*Department of Astronomy, School of Physics, Peking University, Beijing 100871, China*

³*Cavendish Laboratory, University of Cambridge, 19 J. J. Thomson Ave., Cambridge CB3 0HE, UK*

⁴*Kavli Institute for Cosmology, University of Cambridge, Madingley Road, Cambridge CB3 0HA, UK*

⁵*Dipartimento di Fisica e Astronomia, Università degli Studi di Firenze, Via G. Sansone 1, 50019 Sesto Fiorentino, Italy*

⁶*INAF Osservatorio Astrofisico di Arcetri, Largo Enrico Fermi 5, 50125 Firenze, Italy*

⁷*Research Center for Space and Cosmic Evolution, Ehime University, 2-5 Bunkyo-cho, Matsuyama 790-8577, Japan*

⁸*Universidade do Vale do Paraíba. Av. Shishima Hifumi, 2911, CEP: 12244-000, São José dos Campos, SP, Brazil*

⁹*Observatoire de Genève, Université de Genève, 51 Ch. des Maillettes, 1290 Versoix, Switzerland*

¹⁰*Institute of Astronomy, Madingley Rd, Cambridge CB3 0HA, UK*

¹¹*Leibniz-Institut für Astrophysik Potsdam, An der Sternwarte 16, 14482 Potsdam, Germany*

(Received; Revised; Accepted)

Submitted to ApJ

ABSTRACT

Deep observations have detected extended Ly α emission nebulae surrounding tens of QSOs at redshift 2 to 6. However, the metallicity of such extended haloes is still poorly understood. We perform a detailed analysis on a large sample of 80 quasars at $z \sim 3$ based on MUSE-VLT data. We find clear evidence of extended emission of the UV nebular lines C IV $\lambda 1549$ and He II $\lambda 1640$ for about 18% of the sample, while C III] $\lambda 1909$ is only marginally detected in a few objects. By stacking the cubes we detect emission of C IV, He II and C III] out to a radius of about 45 kpc. C IV and He II show a radial decline much steeper than Ly α , while C III] shows a shallower profile similar to Ly α in the inner 45 kpc. We infer that the average metallicity of the circumgalactic gas within the central 30–50 kpc is ~ 0.5 solar, or even higher. However, we also find evidence of a component of the Ly α haloes, which has much weaker metal emission lines relative to Ly α . We suggest that the high metallicity of the circumgalactic medium within the central 30–50 kpc is associated with chemical pre-enrichment by past quasar-driven outflows and that there is a more extended component of the CGM that has much lower metallicity and likely associated with near-pristine gas accreted from the intergalactic medium. We show that our observational results are in good quantitative agreement with the expectations of the FABLE cosmological simulations.

Keywords: quasars: emission lines — galaxies: high-redshift — galaxies: circumgalactic medium

1. INTRODUCTION

Within the circumgalactic medium (CGM), gas and metals are ejected from galaxies by feedback processes, or stripped from infalling satellites. The CGM also hosts the reservoir of metal poor gas accreted from the intergalactic medium (IGM) that can eventually accrete on galaxies to fuel star formation. The matter and energy exchange between the IGM, CGM and galaxies is critical in understanding galaxy star formation, enrichment history and morphological type. Investigating the CGM

and understanding its connection to the star formation activity and interstellar medium (ISM) in galaxies are important to understand galaxy evolution.

A common method to study the CGM is the analysis of absorption signatures against bright background sources (e.g., Rauch & Haehnelt 2011; Matejek & Simcoe 2012; Turner et al. 2014; Lehner et al. 2015; Rubin et al. 2015; Bowen et al. 2016; Martin et al. 2019). This method is sensitive to low column densities, and its detection limit does not depend on redshift or on host

galaxy luminosity (Tumlinson et al. 2017). This method only provides one dimensional (1D) information, and it is limited by the sparseness of background sources. However, it still provides statistical constraints on the CGM if the samples are large enough.

Another method to study the CGM is to directly image a galaxy and its surrounding nebular emission. Directly mapping the CGM is challenging, because its emission is usually weak. Locally several studies have exploited HI 21cm radio emission or soft X-ray emission (e.g., Humphrey et al. 2011; Putman et al. 2012; Anderson et al. 2016). At high redshift most studies have mostly focused on ultraviolet (UV)/optical wavelengths, particularly using the Ly α line. By using the narrow band (NB) technique, tens of individual galaxies and active galactic nucleus (AGNs) have been observed (e.g., Matsuda et al. 2011; Cantalupo et al. 2014), and diffuse Ly α blobs have been detected on spatial scales of tens or even hundreds of kpc. With integral field spectrograph facilities such as the Multi Unit Spectroscopic Explorer (MUSE; Bacon et al. 2010) of Very Large Telescope (VLT), several Ly α nebulae have been detected around quasars and, more recently, also around galaxies (Borisova et al. 2016; Farina et al. 2017; Arrigoni Battaia et al. 2018; Ginolfi et al. 2018; Cai et al. 2018; Arrigoni Battaia et al. 2019a; Drake et al. 2019). These studies achieved a high detection rate of Ly α nebulae, and provided a robust sample for studying the properties of the CGM. Ly α emission is very bright, and it is physically extended due to its resonant nature. The extended Ly α emission could be used to detect the properties of the CGM or even the cosmic web (e.g. Witstok et al. 2019; Arrigoni Battaia et al. 2019b; Lusso et al. 2019). At lower redshift, similar observations have been undertaken to search for extended emission of different transitions such as H α or [O III] $\lambda\lambda$ 4959,5007 (Schirmer et al. 2013; Yuma et al. 2017, 2019).

Metals provide an important tracer to probe the interconnection between the IGM, CGM and galaxies. Metals are produced inside galaxies, but the bulk of them have been distributed outside galaxies across the cosmic epochs. Peebles et al. (2014) performed a census of metals in and around star-forming galaxies in the local Universe. They reported a surprisingly small fraction (20%–25%) of metals remaining in stars, interstellar gas, and interstellar dust. Recent overviews of the metal budget in and around galaxies are given in Tumlinson et al. (2017) and Maiolino & Mannucci (2019). Metals are transferred to the CGM via processes such as outflows and stripping (e.g. Tremonti et al. 2004; Tripp et al. 2011; Tumlinson et al. 2017). The metal enrichment of the CGM provides information about the origin

of the CGM gas. Metal poor gas in the CGM possibly suggests pristine IGM accretion (Chen et al. 2019), while metal-rich components of the CGM are likely associated with large-scale galactic outflows (Muratov et al. 2017; Chisholm et al. 2018).

Numerous cosmological simulations can predict the metallicity distribution and evolution in the CGM (e.g. Nelson et al. 2018; Crain et al. 2013; Vangioni et al. 2018). However, these predictions are subject to various uncertainties, such as the supernova and AGN feedback efficiency, the metal loading and advection in the outflows, and mixing with the gas inflowing from the IGM. Therefore, observational constraints of the CGM metallicity are crucial to understand the physics of galaxy formation.

After Ly α , the brightest UV emission lines from gas photoionized by quasars are C IV λ 1549, He II λ 1640 and C III] λ 1909 and, sometimes N V λ 1240 (hereafter C IV, He II, C III], N V, respectively), either in their host galaxy or in the CGM. Their line ratios are often used to constrain metallicity, ionization parameter, and gas density (Nagao et al. 2006; Gutkin et al. 2016; Maseda et al. 2017; Matsuoka et al. 2009, 2018; Mignoli et al. 2019; Dors et al. 2014, 2018, 2019).

While previous studies have focused on the Ly α distribution and kinematics, in this paper we investigate the nature of the CGM in a large sample of $z = 3 - 4$ quasars by using the strength of UV lines, e.g., C IV, He II and C III] (which have been little explored in previous studies), with the ultimate goal of constraining the metallicity of the CGM. At these redshifts these lines are shifted into the MUSE wavelength range. This approach follows similar analysis methods undertaken for Ly α nebulae around quasars at $z \sim 3$ (e.g. Borisova et al. 2016; Ginolfi et al. 2018; Arrigoni Battaia et al. 2019a), but focusing on the diffuse nebulae of these faint UV lines, which are obviously much more difficult to detect and map relative to Ly α and, as a consequence, we also have to rely on the use of data stacking.

The structure of our paper is as follows. In Section 2, we describe our data and data reduction procedure. In Section 3 we present our results. We discuss the implications of our findings in Section 4. Section 5 summarizes our results. Throughout this paper, we adopt the standard Λ CDM cosmology with $H_0 = 70 \text{ km s}^{-1} \text{ Mpc}^{-1}$, $\Omega_m = 0.3$ and $\Omega_\lambda = 0.7$. All distances are proper, unless specially noted.

2. DATA DESCRIPTION AND ANALYSIS

In this section, we analyze a large and deep MUSE sample of 80 quasars at $z \sim 3$ taken from the archive. The sample combines two large samples from Borisova

et al. (2016) and Arrigoni Battaia et al. (2019a). Both papers aim to detect the Ly α nebulae around quasars. In our work, we focus on the other UV emission lines within the MUSE wavelength range, such as C IV, He II, and C III]. These emission lines are generally too weak to get individual detections in most targets, but with this large sample we can at least obtain a stacking result. The Borisova et al. (2016) sample includes 17 radio-quiet quasars and 2 radio-loud quasars. The Arrigoni Battaia et al. (2019a) sample consists of 61 quasars, including 15 radio-loud quasars. The total exposure time is ~ 97 hrs, about 1.2 hrs for each object on average. The quasars in the sample are listed in Table 1, along with some of their physical properties.

We downloaded all the processed and calibrated datacubes of the sample from the ESO Archive. Residual background emission was removed from each wavelength slice of the cube by determining the average residual sky emission in a meshed grid, avoiding the central $5''$ around the quasar. The inferred background emission was interpolated spatially, also beneath the location of the quasar. We carefully checked that this procedure did not subtract the diffuse nebular emissions. In this procedure, we intended to eliminate the uneven background, which is insignificant in the original datacubes, but becomes relevant after subtraction of the quasar light, as discussed in Section 2.1.

We note that the ESO pipeline is claimed to be suboptimal with respect to other non-public pipelines developed by other groups (e.g. those used in Borisova et al. 2016; Arrigoni Battaia et al. 2019b), however we have verified that the final rms (especially for the stacks), after the refined background subtraction, is similar to the one obtained in those papers.

2.1. PSF and Continuum Subtraction

As the emission from the central AGN is much brighter than the diffuse emission of the CGM, an important step is to remove the unresolved AGN emission from the spatially resolved emission of the CGM. To do this, we took advantage of the integral field spectroscopic information delivered by MUSE. We used the wavelength regions where we were sure that no extended line emissions should be present. To estimate and remove the quasar PSF, we adopted a purely empirical method similar to that introduced in Borisova et al. (2016). For each wavelength layer, we produced a pseudo-NB image with a spectral width of $\sim 187\text{\AA}$. The empirical PSF is rescaled to match the flux within the central 5×5 pixels ($1'' \times 1''$). To avoid the contamination of cosmic rays or other artifacts, an averaged-sigma-clip algorithm was applied to calculate the scaling factor

between the flux of the central quasar in each layer and the PSF images. We then cut the central circular region of the PSF image within a radius of five times the seeing, and subtracted it from the original datacube. This method provides good results, but the central $1'' \times 1''$ region used for PSF rescaling is not usable as the flux in this region must be zero by construction. We therefore masked the central $1'' \times 1''$ region in our study as we are interested in emission on larger scales. Note that the PSF at the wavelength of the nebular lines was constructed by interpolation of the PSF inferred from the nearby continuum channels.

Next, we adopted a median-filtering approach to remove continuum sources in the datacube, as described in Borisova et al. (2016). This approach provides a fast and efficient way to remove continuum sources in the search for extended line emission. We also masked several bright neighboring objects to avoid possible contamination. The subtraction of PSF and continuum emission was done for each exposure. We stacked different exposures of the same object, by spatially re-aligning the cubes, weighted by their exposure time.

In order to improve the signal to noise (S/N) and to obtain the average radial profile we also adopted two different stacking methods that will be described in Section 3. For the stacking, in order to further improve the sensitivity, we have masked the wavelengths affected by strong OH lines, prior to the shifting to the wavelength rest frame and prior to averaging the cubes.

2.2. Line Emission Extraction

The final step is to extract and identify the extended line emission from the PSF and continuum subtracted datacubes. The extraction was performed based on a S/N threshold on each individual spectral slice of the cube. Voxels with S/N lower than 1 were masked. Note that this is a S/N threshold much more conservative than that used in other works. For instance, Borisova et al. (2016) adopt a S/N threshold of 2 on spaxels spatially smoothed with a Gaussian filter with a $\sigma = 0.5''$, which is equivalent to a S/N threshold of 0.34 on individual unsmoothed spaxels. The S/N threshold results into a three dimensional (3D) mask for each datacube and, finally to obtain a “S/N clipped” datacube. Then we applied pseudo-NB filters to the wavelength ranges of C IV, He II, and C III] by summing up the flux along the wavelength axis for pixels selected by the 3D masks (i.e. only those pixels meeting the S/N threshold requirement in each slice). The width of each pseudo-NB filter is about 30\AA in rest-frame around the line centre. Finally we obtain the pseudo-NB image of each emission line.

We verified that the UV lines detected (or even marginally detected at 2σ) are not residuals of the quasar light PFS subtraction by verifying that they are much narrower than the quasar emission lines, that they are not spatially radially symmetric, and that they are well above the signal measured in the neighbor continuum emission profile. These tests will be clarified further especially in the case of the stacked emission.

An accurate systemic redshift is important to detect UV line emission and kinematics and also for accurately shifting the spectra to the same rest-frame for stacking multiple spectra and cubes from different quasars. For quasars at $z > 2$, an accurate measure of systemic redshift is hard to achieve, and generally relies on the observations in near infrared or molecular tracers (e.g., McIntosh et al. 1999; Venemans et al. 2017). We could get the corrected redshift estimated from the broad C IV line, but the intrinsic uncertainty is about $\sim 400 \text{ km s}^{-1}$ (Shen et al. 2016), which is too large for the requirements of diffuse line detection. Therefore, in this paper, we used the redshift estimated from the diffuse Ly α nebulae, i.e. the narrow and extended component of Ly α . There could be a velocity offset between the peak of the Ly α nebulae emission and the systemic redshift (e.g., Arrigoni Battaia et al. 2019a), however these shifts are generally small, because the CGM gas traced by Ly α is characterized by relatively quiescent kinematics. For the objects that have clear detections of diffuse C IV, He II, or C III] nebulae, we found that the redshifts of diffuse Ly α nebulae (calculated by the spectrum extracted in $3''$) is consistent with those of C IV, He II, or C III]. Therefore, we use the redshifts of diffuse Ly α as the systemic redshifts of the quasars.

Note that also for the extraction of the line maps the wavelengths of strong OH lines were masked to improve the sensitivity.

3. RESULTS

3.1. Extended UV Emission Line Haloes

Following the reduction steps in Section 2, we detect Ly α , C IV, He II, C III] nebulae extended on circumgalactic scales around a subset of individual quasars in our sample. Line maps of four objects for which we can detect and resolve both C IV and He II are shown as examples in Figure 1. The scale of the thumbnails is $20'' \times 20''$ (corresponding to $150 \times 150 \text{ kpc}$ at the median redshift of the sample). All these four quasars are radio-quiet. For convenience, the number on the top left corner of each image indicates the ID of each targets listed in Table 1. The atlas of emission line maps of all detected nebulae are shown in Figures A.1, A.2, A.3 and A.4 in Appendix A, for Ly α , C IV, He II and C III],

respectively. Radio-loud quasars are marked with open circles.

The detection rate of Ly α nebulae is 100% for our sample of quasars, which has already been reported by Borisova et al. (2016) and Arrigoni Battaia et al. (2019a). All 4 objects presented in Figure 1 show enormous and asymmetric Ly α nebulae. It is not clear whether the morphology of these Ly α blobs reflects the distribution of the CGM or the way with which the CGM is illuminated by the (anisotropic) light of the quasar.

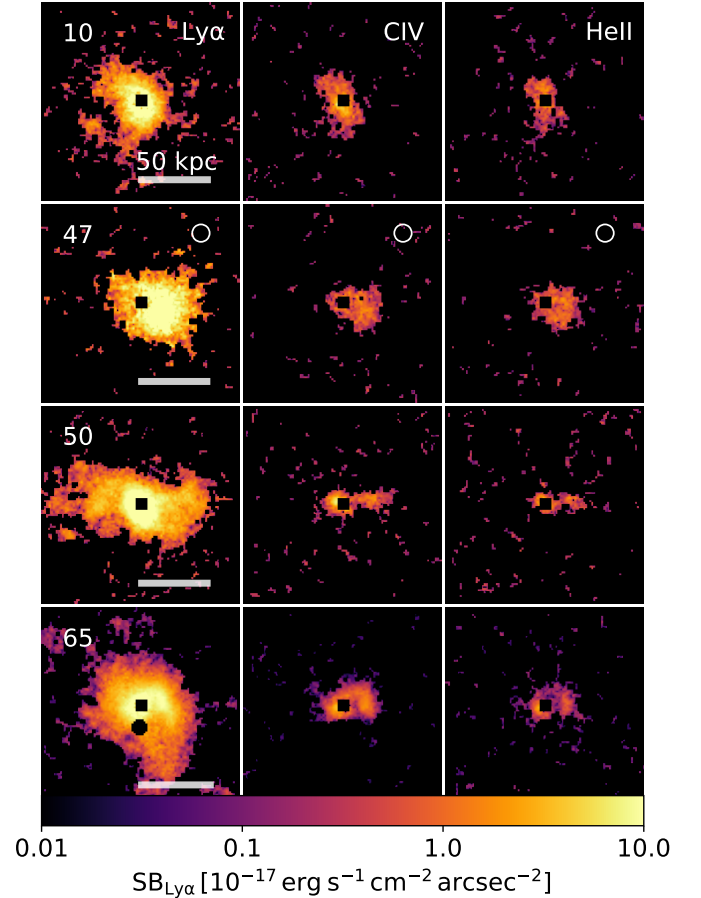


Figure 1. Maps of the Ly α , C IV and C III] emission for four quasars that show extended emission of both C IV and He II (No. 10, 47, 50, 65 in Table 1). In each panel, the original position of each quasar is masked by a small ($1'' \times 1''$) black square. Each thumbnail has a size of $20'' \times 20''$, corresponding to about 150 kpc at the median redshift of the sample. These images are produced by collapsing S/N-clipped datacubes with 3D masks along the wavelength direction.

In Figure 1, C IV nebulae are more compact than their Ly α counterparts for all four objects. This effect is certainly partly due to the C IV line being fainter and therefore its detectability threshold is reached at smaller radii; however, in Section 3.3 we will show that

the C IV radial profile is indeed steeper than Ly α . In total, extended C IV emission is detected for 15 quasars, as shown in A.2. Among these 15 quasars detected in extended C IV, 4 are radio loud, and 11 are radio quiet.

The He II morphology is generally similar to that of C IV, as is shown in Figure 1, which is not surprising given that they have comparable ionization potentials. Over all 80 quasars, extended He II emission is detected for ten of them, as shown in Figure A.3. Three objects are radio loud, and the others are radio quiet. The C IV and He II nebulae span a range of diverse morphologies in the sense that most of them are asymmetric, similar to the shapes of their Ly α nebulae. The examples in Figure 1 show clear filamentary/elongated shapes.

The diffuse C III] emission is much fainter than C IV and He II. None of the four objects shown in Figure 1 is detected with diffuse C III] emission. Within the whole sample, only 4 objects are detected with extended C III] emission, with of of them being radio loud, as shown in Figure A.4. For objects at redshift 3 to 4, the C III] line is redshifted to a wavelength range affected by several OH sky lines. Therefore, the C III] data are noisier, and it is difficult to obtain reliable measurements of their nebular morphology.

N V is hardly detected, but at this wavelength there are more problems in properly removing the contribution from the strong and broad profile of the Ly α from the Broad Line Region (BLR) of the quasar and also the underlying continuum, which has a discontinuity around Ly α due to IGM absorption. These are obviously issues also for Ly α , but are more relevant for NV as it is much fainter than Ly α . Anyhow, as discussed in Nagao et al. (2006), the diagnostics involving nitrogen are more difficult to interpret as they rely on the assumed nitrogen abundance scaling with respect to other elements, which is poorly known in AGNs and especially at high redshift (see Dors et al. 2017, 2019, and references therein).

3.2. Line Ratios Diagnostics and Metallicity

We use the C IV, He II, and C III] emission to estimate the metallicity of the CGM gas based on AGN photoionization models. C IV, He II, and C III] are lines whose ratios have been commonly applied to estimate the metallicity and ionization conditions in radio galaxies, AGNs and star forming galaxies (e.g. Nagao et al. 2006; Dors et al. 2014; Matsuoka et al. 2018; Dors et al. 2019; Mignoli et al. 2019; Gutkin et al. 2016; Nakajima et al. 2018; Pérez-Montero & Amorín 2017).

We first use the models provided by Nagao et al. (2006) and Matsuoka et al. (2018). These models are mainly based on the CLOUDY models, using a typical quasar-like ionizing continuum, spanning a wide range of

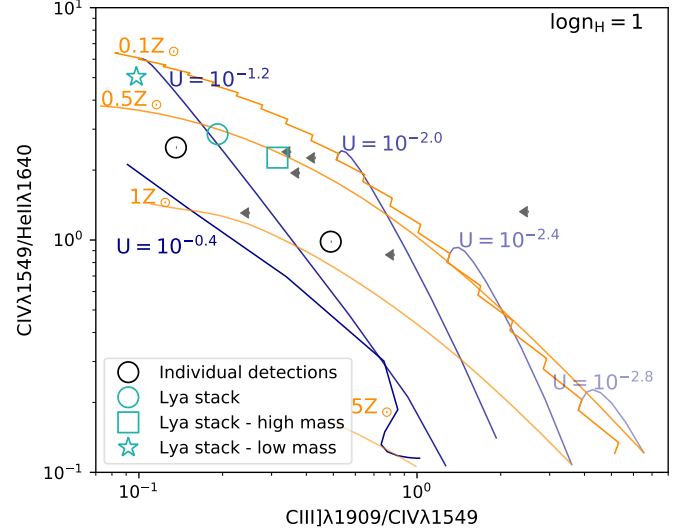


Figure 2. C IV/He II vs C III]/C IV diagnostic diagrams. Lines show the results of quasar photoionization models at fixed ionization parameter (blue) and at fixed metallicity (orange). The gas density of the model is $\log n_H = 1$. Black open circles show the line ratios of the only two quasars with detection of extended emission for all three lines, C IV, He II, and C III]. Black triangles show the upper limits of objects with C IV and He II detections, but without C III] detections. The light blue circle shows the result of stacking all spaxels with Ly α detection. The results obtained by splitting the sample in high-mass and low-mass BHs are shown with a square and a star, respectively.

metallicities and ionization parameters. Figure 2 shows the grid of ionization models for a range of gas metallicities and ionization parameters. The blue and orange lines show models at constant ionization parameter and at constant metallicity, respectively. These models are obtained assuming a gas density $n_H = 10 \text{ cm}^{-3}$, which is appropriate for the clumpy gas on large (kpc) scales in the circumgalactic medium which is responsible for the bulk of the nebular line emission under investigation; we will further support this choice (and show that it is a conservative assumption) through the guidance of cosmological simulations as discussed in Section 4.3. Typically, the inner Narrow Line Region (NLR) of AGNs have even higher densities (e.g. Mingozi et al. 2019), which would result in metallicities even higher than estimated in the following (Nagao et al. 2006; Matsuoka et al. 2009). Recent spatially resolved observational studies (e.g. Revalski et al. 2018) have shown that the electron density in some NLRs decreases with the radius. However, Dors et al. (2019) found that electron density variations as a function of distance from the AGN have an almost negligible influence on the predicted line ratios and, consequently, on metallicity estimations.

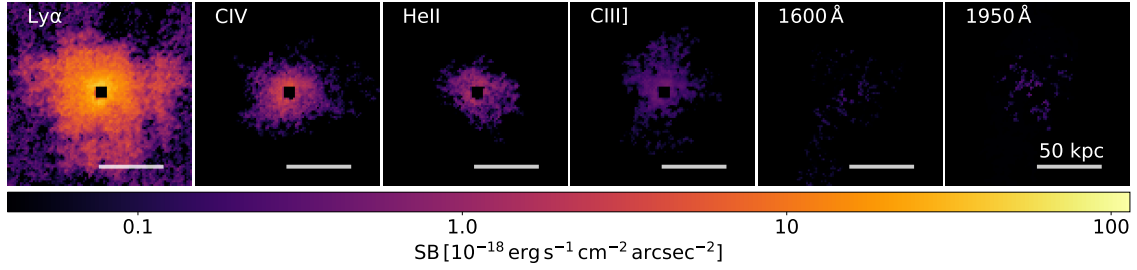


Figure 3. Maps of Ly α , C IV, He II and C III] resulting from the stacking of all MUSE cubes. We also plot the residuals of the continuum emission at 1600Å and 1950Å for comparison. Each thumbnail has the same size as in Figure. 1.

We only have two objects with detections of all three emission lines. They are shown as the open circles in Figure 2. Their line ratios fall in the region with a metallicity $0.5Z_{\odot} < Z < Z_{\odot}$. For the objects with C IV and He II detections but without C III] detections, we provide the upper limits of the C III]/C IV ratios, as shown by the black triangles. These result into metallicity lower limits in the region of $0.1Z_{\odot} < Z < 1Z_{\odot}$. It should be noted that the line flux for these individual objects is measured within a $3''$ aperture, which traces a relatively central region of about 8–24 kpc.

In order to maximize the S/N and make an assessment of the average properties of Ly α nebulae, we stack all the spaxels with detection of Ly α for all 80 objects together. To examine possible trends, we split the sample based on the black hole mass of the individual quasar, computed from the quasar continuum luminosity at 1450Å and FWHM of C IV, following the virial method given in Trakhtenbrot & Netzer (2012). Since most of the nebulae are faint, we simply divide the sample into two halves. The inferred black hole masses for individual objects are listed in Table 1. The median value of black hole mass is $10^{10.26} M_{\odot}$. The line ratios resulting from stacking all 80 objects is shown with the light blue circle in Figure 2. The high-mass and low-mass subsamples are indicated with a square and a star, respectively. The average metallicity for the Ly α nebulae resulting from the stacking of the whole sample is about $0.5Z_{\odot}$, smaller than the two individual detections shown by black circles. The properties of high-mass and low-mass subsamples are quite similar, with the low-mass subsample having slightly lower metallicity, which is likely mirroring the mass-metallicity relation at these redshifts (Maiolino et al. 2008; Troncoso et al. 2014; Onodera et al. 2016) extending also to quasars (Matsuoka et al. 2011; Xu et al. 2018) and on large scales (but see Mignoli et al. 2019).

We have also interpreted the line ratios by using the photoionization models presented by Dors et al. (2019), that derived two semi-empirical calibrations between the metallicity of the NLR of type-2 AGN and the rest frame of the N V/He II, $C43 = \log[(C\text{ IV} + C\text{ III}]/\text{He II}]$, and

C III]/C IV emission-line intensity ratios. We use their C43 versus C III]/C IV diagram to derive the metallicities of the CGM in our sample. With those models we obtain even higher, super-solar metallicities for the two objects with detections of all three emission lines. Specifically, we find metallicities in the range 2–4 Z_{\odot} and ionization parameter $\log U$ in the range between -1.5 and -1.0 .

3.3. Average Radial Profiles from Stacking

Despite the deep observations of the quasars in our sample, we only directly detect the C IV, He II, and C III] emission lines from the CGM for a small fraction of the quasars. To determine the average line strengths and obtain spatially resolved information on the properties of the CGM we adopt a full 3D-cubes stacking procedure. We apply this procedure to the datacubes after the PSF and continuum subtraction. We shift individual datacubes and re-bin them to a common (rest-frame) wavelength frame. The cubes are also re-aligned spatially to the position of the quasar continuum position. The cubes are averaged and weighted by their exposure time. We visually inspect each datacube to avoid contamination from bright stars and other artifacts in the field of view. We have also stacked the cubes by taking their median and the result is almost indistinguishable from the average-stacked one. Finally, we dynamically extract the stacked nebular line emission maps following the procedure described in Section 2.2, i.e. extracting pseudo-NB images after masking each pixel in the cube by the same S/N threshold given in Section 2.2.

The resulting maps of Ly α , C IV, He II, and C III] are shown in Figure 3. A clear, large average Ly α nebula is visible, and fainter but clear C IV, He II and C III] nebulae are also seen.

We measure average radial profiles from these line maps by extracting the flux averaged in radial annuli. The top panel Figure 4 shows the average radial surface brightness profile for Ly α , C IV, He II, and C III] in blue, orange, green, and red, respectively. We also plot the radial profile of PSF-subtracted continuum residuals in the

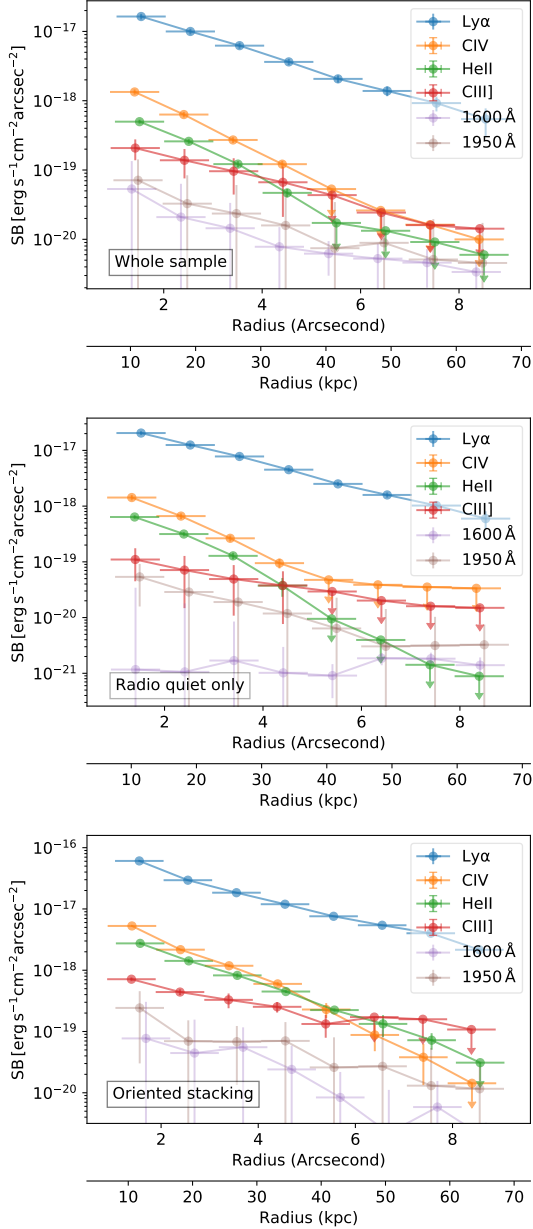


Figure 4. Average surface brightness profiles of the nebular lines for the stacked datacubes. For comparison, the radial profiles of PSF continuum subtraction residual at 1600Å and 1950Å are also shown. The top panel shows the result of stacking all cubes of all quasars. The central panel shows the result of stacking only radio quiet quasars. The bottom panel shows the profile extracted along a pseudo-long slit on the stack obtained after re-aligning the cubes along the Ly α extension. In each panel, the bottom scale gives the radius in kpc at the median redshift of the sample.

wavelength range between C IV and He II (i.e. 1600Å) and at a wavelength just next to CIII] (specifically at 1950Å). Since there are no prominent nebular lines at these wavelengths and the continuum extended emission

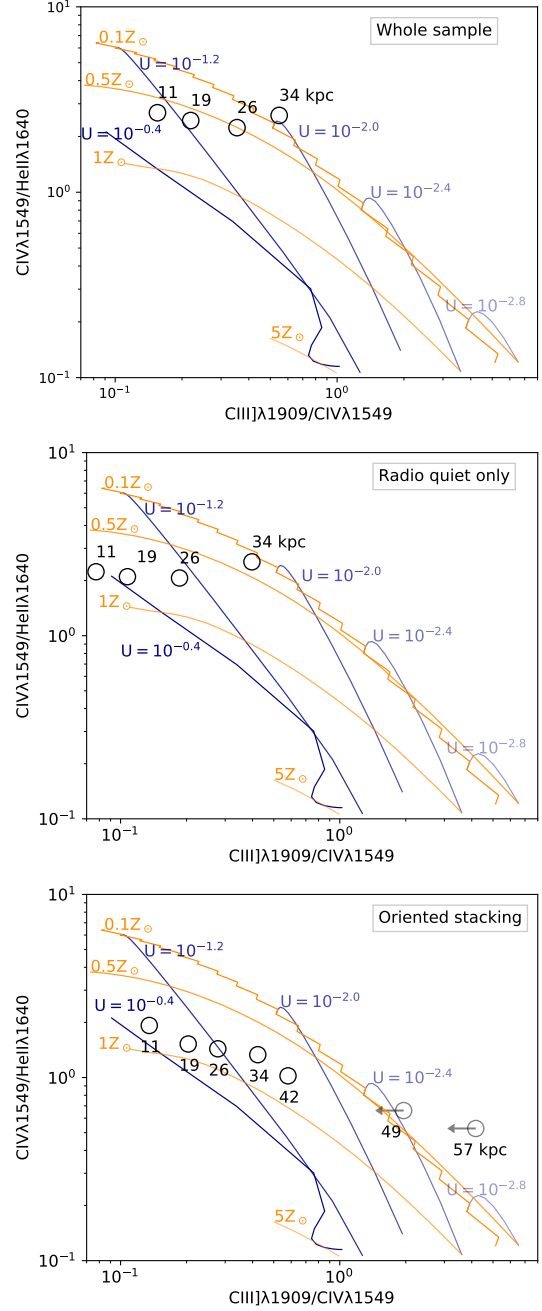


Figure 5. The same diagnostic diagram as in Figure 2 for the line ratios inferred from the stacked cubes. The open circles in different colors show the line ratios at different distances from the center. The distance is given in kpc next to each symbol. The top panel shows the result from the stacking of all cubes of all quasars. The central panel shows the result of stacking only radio quiet quasars. The bottom panel shows the line ratios extracted from the pseudo-long slit one the stack obtained after re-aligning the cubes along the Ly α extension.

should be negligible, the emission at these wavelengths is likely only associated with residuals from the PSF

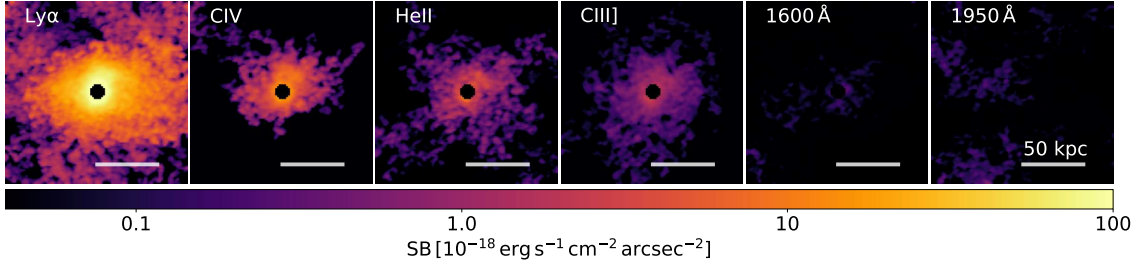


Figure 6. Maps of Ly α , C IV, He II, C III], and residuals at 1600Å and 1950Å, obtained from the cubes stacked after re-aligning them along the primary Ly α extension. Each thumbnail has the same size as in Figure. 1.

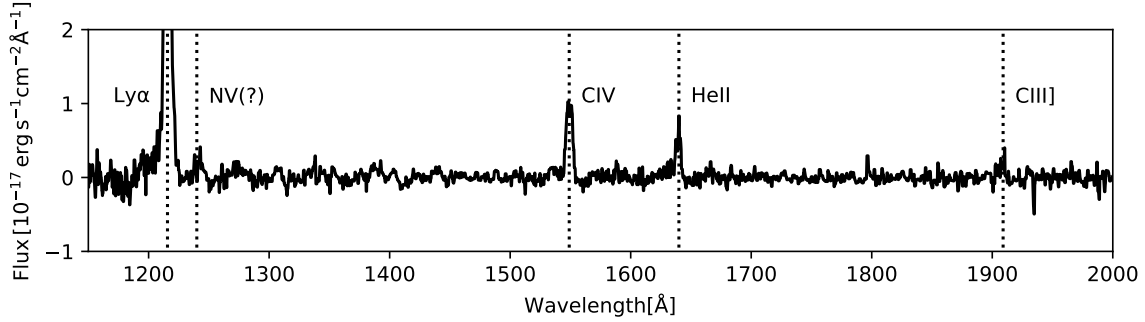


Figure 7. The 1D spectrum extracted by a pseudo long slit on the cube obtained by staking the individual cubes along the primary Ly α extension.

subtraction or from residual sky emission (in particular residual, unmasked OH emission lines) and therefore gives us a measure of the reliability of the detection of the nebular lines.

As illustrated in the top panel of Figure 4, the Ly α surface brightness is about one order of magnitude higher than that of C IV, He II, and C III], and the gap is even larger at larger radii. The average profile of C IV and He II is also about one order of magnitude brighter than the PSF subtraction residual at 1600Å. This means our results are reliable. The C III] radial profile is closer to the 1950Å continuum residual radial profile, indicating that the detection of this line is indeed more marginal, at the 2σ level (the detection will become more significant with the approach discussed in the next section when aligning the nebulae). Beyond a radius of 5 arcsec (~ 40 kpc) none of the emission lines, except for Ly α , is detected.

The C IV radial profile is steeper than the Ly α profile, which could be naively interpreted as radially decreasing metallicity. However, the He II has the same steep radial profile as C IV, which suggests that the decrease of these two lines is more a consequence of a decreasing ionization parameter as a function of radius (which is expected if the gas density decreases more slowly than r^{-2}). The C III] line, despite being more marginally detected, decreases less steeply than C IV and He II, and

follows a similar decline as Ly α . This reinforces the idea that the radial variation of metallicity is not strong.

We also repeat the stacking and profile extraction excluding the radio-loud quasars. As it has been claimed that metal lines in the CGM are perhaps associated with (rare) radio jets (Borisova et al. 2016), by excluding those few radio loud quasars in the sample we can assess if the result is potentially dominated by the few radio loud sources. The resulting nebular lines profiles obtained by stacking only the radio-quiet quasars are shown in the central panel of Figure 4. There are no significant differences with respect to the result obtained by stacking the whole sample (top panel). The main difference is for the upper limits at large radii that, in the case of staking only the radio-quiet quasars, are less constraining.

Figure 5 shows the diagnostic line ratios at different radii resulting from the cube staking. The line ratios at different distances are shown by colored circles and the physical distances are labelled next to each circle. The top panel shows the result from stacking the whole sample while the central panel is the result from stacking only the radio-quiet quasars. The metallicity remains stable at about $0.5Z_{\odot}$ out to <30 kpc, while the ionization parameter decreases, as expected. The diagnostics measured at 34 kpc suggest that both metallicity and ionization parameter decrease at even larger radii.

3.4. Profiles Along the Ly α Extensions

In Section 3.1 we have shown that most strong Ly α nebulae are not radially symmetric and that the shapes of their C IV, He II, and C III] nebulae are, in general, similar to their Ly α counterparts. Therefore, a random stacking of datacubes is not an efficient way to enhance the S/N at large distances. Moreover, the random stacking may result into a biased result, in the sense that the presence of clumps with high metallicity and high surface brightness may be washed out by the random averaging method. In this section we stack the nebular emission by re-aligning them along the direction of the primary Ly α extension.

We select 15 objects that have very extended and asymmetric Ly α nebulae (IDs 8, 10, 13, 18, 21, 33, 47, 49, 50, 51, 56, 65, 67, 74, 75). Note that in this case we also include for completeness 4 radio loud quasars, as they are among those showing asymmetric extended nebulae, but the results do not change significantly by excluding these four objects. We find the major axis for each target according to the shape of Ly α nebulae via a principal component analysis (PCA). For each Ly α image, we calculate its covariance matrix, eigenvectors, and eigenvalues. Then we align each datacube horizontally based on the major axis via a linear transformation. The rotating transformation matrix is calculated by the major eigenvector. We then proceed with the same stacking procedure discussed in the previous section using the re-aligned cubes.

Figure 6 shows the line maps resulting from the re-aligned stacked cubes. In each map, the surface brightness distribution is obviously stretched in the horizontal direction, especially in Ly α . Note that the outer boundaries of the nebulae are now more irregular and noisier than in the maps from the global stacking as a consequence of the much smaller number of haloes being combined here. We apply a horizontal pseudo-long slit with a width of 20 spaxels to the stacked datacube. We only use the data in this slit and avoid other areas with little signal (which would contribute primarily only with noise and sky residual emission). Using this method we cannot obtain a truly average radial surface brightness distribution, but the average properties for such regions along the extended Ly α emission. The 1D spectrum extracted from such a pseudo-slit are shown in Figure 7, which clearly reveals the detection of C IV and He II. C III] is more marginally detected, but significant, as discussed in the following. NV may also be detected, but as already mentioned in this spectral region potential systematic residuals from the strong broad Ly α emitted by the quasar BLR makes the spectral features uncertain and questionable.

The nebular lines radial profiles along the Ly α extension are shown in the bottom panel of Figure 4. As expected, the surface brightness of all nebular lines is significantly enhanced compared to the average results shown in Figure 4. The S/N is higher, including for C III], which is better detected. The significance of the detection for all lines is confirmed by the comparison with the radial profiles of the residuals extracted at 1600Å (for C IV and He II) and at 1950Å (for C III]). The detections now extend to larger distances of about 5 arcsec (corresponding to about 45 kpc at the average distance of these quasars).

Also in this case C IV and He II decrease more steeply than Ly α while C III] shows a flatter profile, again supporting the idea that the bulk of the decrease of the C IV and He II is primarily due to the ionization parameter, while the metallicity does not change dramatically.

We derive the metallicity and ionization parameter of the gas along the Ly α extension in the bottom panel of Figure 5. The metallicity of these regions stays stable at $0.5Z_{\odot} < Z < Z_{\odot}$ out to about 42 kpc, but the ionization parameter decreases with the distance, as expected. It is not surprising that the metallicity in this case is higher than in the randomly oriented stacking. Indeed, as already mentioned, along the Ly α extension we are probably tracing gas that has been enriched more recently by the quasar outflow, as quasar-driven outflows and direction of quasar illumination are generally in the same direction.

3.5. Kinematics

We use the “S/N clipped” datacube defined in Section 2.2 to produce the two dimensional maps of flux-weighted velocity centroid and flux-weighted velocity dispersion. We do not fit any emission line profile, but produce the first and second momentum of the flux distribution in the wavelength domain. The first and second momentum maps then indicate the velocity and velocity dispersion, respectively. The velocity and velocity dispersion maps of Ly α nebulae have been published in Borisova et al. (2016) and Arrigoni Battaia et al. (2019a). In this section, we therefore focus on the kinematics of C IV and He II, and only on the four large nebulae in which the kinematics can be fully resolved with a good S/N (ID 10, 47, 50, 65). C III] is too noisy and barely resolved in any individual object to have the kinematics properly mapped.

Figure 8 shows the resulting velocity field and velocity dispersion inferred from Ly α , C IV, and He II. As discussed in Section 3.1, C IV and He II are much fainter and more compact than Ly α , only tracing the central region. Ly α traces large scale motions that are diffi-

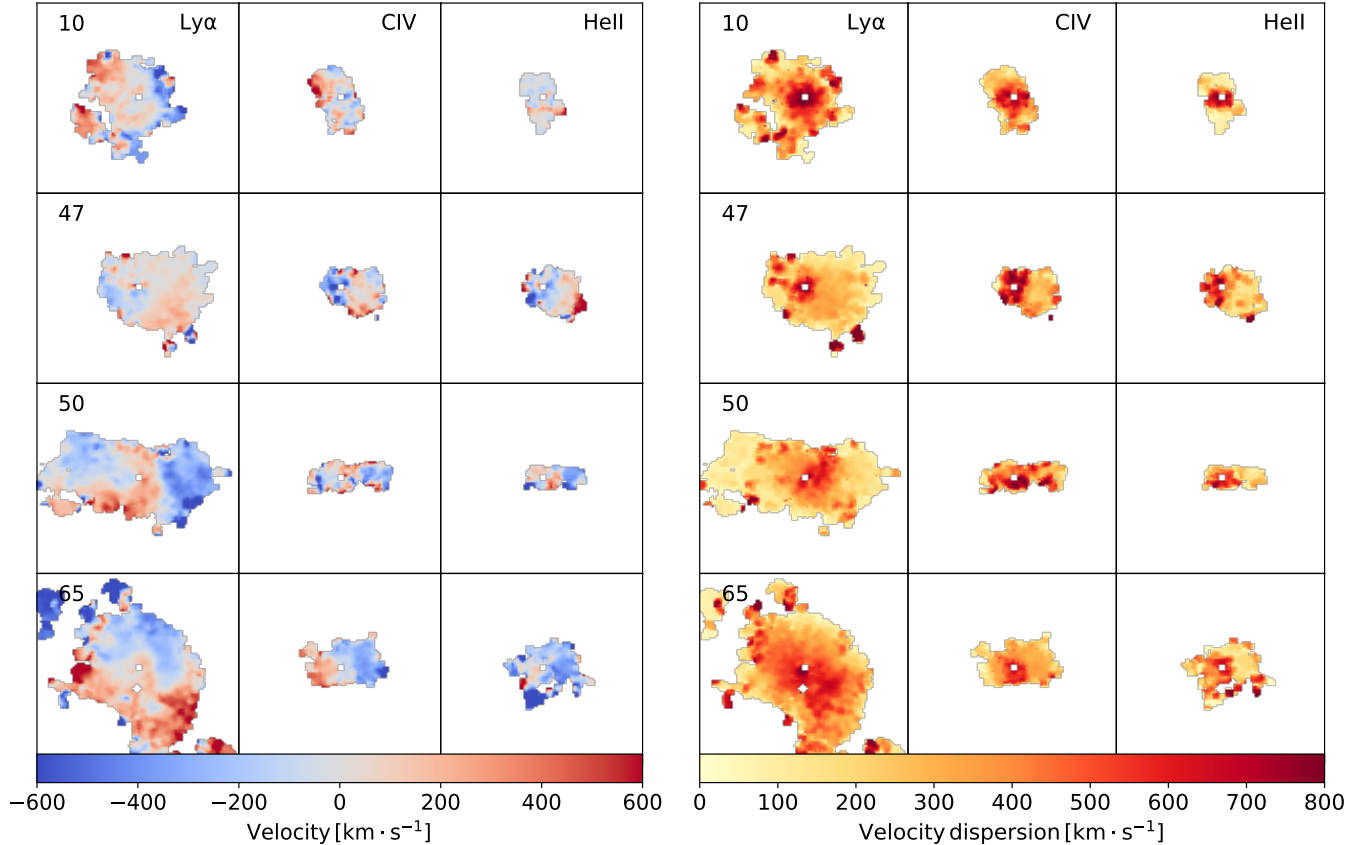


Figure 8. Projected velocity field (left panel) and velocity dispersion (right panel) traced by Ly α (left column), C IV (middle column), and He II (right column) of the same four objects shown in Figure. 1. The velocity and velocity dispersion are estimated from the first and second momentum of the flux distribution, respectively. Each thumbnail has the same size as Figure. 1.

cult to identify in terms of simple rotation, inflow or outflows, although there are interesting similarities with what is seen in cosmological simulations, as discussed later on. However, here it is interesting to note that C IV and He II broadly share the same velocity pattern as Ly α . The additional interesting aspect is that all three nebular lines are characterized by very large velocity dispersions in the innermost region ($r < 2''$), exceeding 700 km/s, likely tracing active outflows, although we can not exclude this may be tracing the virial motions in the central deep gravitational potential well (this will be discussed further when comparing with the numerical simulations). However, on larger scales the velocity dispersion rapidly drops to much lower values (100–200 km/s) indicating that metal enriched gas on larger scales is dynamically quiescent and likely part of the virialized CGM. A similar kinematic pattern is also observed in a $z \sim 5$ quasar (Ginolfi et al. 2018, Ginolfi et al. in prep).

4. DISCUSSION

4.1. Implications of High Metallicities in the Circumgalactic Medium

The metallicity that we infer for the CGM, out to a radius of about 40 kpc in the stacked spectrum (and also in two individual targets) is far too high ($> 0.5 Z_{\odot}$) to be ascribed to gas recently accreted from the IGM. In past works the detection of extended C IV was associated with radio loud quasars (e.g. Borisova et al. 2016) and generally it is typical for giant Ly α nebulae around high redshift radio galaxies that show high C IV and He II (e.g. Villar-Martín et al. 2007), which might indicate that the high metallicity gas in these systems has been somehow lifted by the motions associated with the jet. However, in our sample only 4 out of 15 objects that have individual C IV detections are radio loud. Moreover, we clearly detected extended metal line emission and high emission also in the stack that excludes radio loud quasars. Also other studies, such as Cai et al. (2017), have found large giant Ly α nebulae with extended C IV and He II emission in galaxy overdensities without any radio detection. Therefore, there must (also) be mechanisms other than jets promoting the transport of metals to the CGM.

Such high metallicities must have resulted from past extensive enrichment from outflows likely coming from the central galaxy, possibly outflows generated by consecutive quasar phases, which we know are capable of ejecting large amounts of highly enriched gas into the CGM especially in the early Universe (e.g. Cicone et al. 2014; Fluetsch et al. 2019; Bischetti et al. 2019; Maiolino et al. 2012; Cicone et al. 2015; Cano-Díaz et al. 2012; Carniani et al. 2015, 2017). Indeed, quasar-driven outflows are fast enough to reach large radii in the halo of the galaxy and dump enough enriched gas, during consecutive active episodes (see discussion in Cicone et al. 2015), so that they can bring the metallicity of the CGM to a value close to solar (or even supersolar), within a radius of 50 kpc, already within the first 2 Gyr. Highly metal-loaded SN-driven winds from the central galaxy may also contribute to the enrichment of the CGM on these scales.

An additional source of metals in the CGM could be the enrichment by satellite star forming galaxies, whose ISM may be ram-pressure stripped in the hotter halo of the central galaxy or dispersed through supernova-driven winds. In the field of view of these objects it is hard to detect any faint satellite galaxies around the quasars, but these may be well below our detection limit and possibly lost in the residuals of the bright quasar light PSF subtraction.

Based on numerical simulations, Hafen et al. (2019) point out that more than half of the CGM mass originates as (near-pristine) IGM accretion, and wind from the central galaxy is the second important contribution. Gas can be detained in the CGM for billions of years, resulting in a well mixed halo. Therefore, the high metallicity CGM we detect is very likely to trace a mixture of pristine or near-pristine accretion from the IGM, and metal-rich outflows from central galaxies or gas stripped from other satellite galaxies. Our results at least qualitatively support this scenario.

4.2. Two Components of the CGM

According to the simulation of Muratov et al. (2017), nearly all metals produced in high redshift galaxies are carried out by galactic winds as far as $0.25R_{\text{vir}}$. At R_{vir} the outflow metallicity is expected to decrease due to the dilution by the metal-poor component part of the CGM more closely associated with the accreting gas from the IGM. In our results, we do detect a possible metallicity decrease for randomly-oriented stacked results at radii larger than 30 kpc (Figure 5). There seems to be, on average, a metal poor component of the CGM exterior to the central, metal rich one. However, the result is

not robust since the signal is extremely weak at large distances.

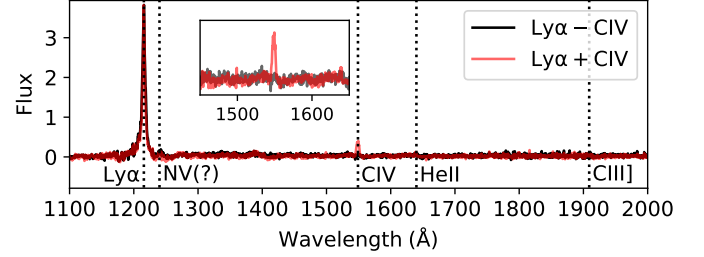


Figure 9. Red line: stacking of all spaxels for all objects with both Ly α and C IV detections. Black line: stacking of all spaxels with Ly α but without C IV detections. The inset shows a zoomed around C IV.

As discussed in the previous section, the larger extension of the Ly α halo with respect to the other UV lines is primarily due to the fact that Ly α is much stronger (and also located in a spectral region in which MUSE is more sensitive and with lower sky background) and therefore can be traced to larger radii from the quasar. The geometrical dilution with radius of the quasar’s photoionization radiation (hence the decrease of ionization parameter) also contributes to the decline of high ionization lines such as C IV and He II. However, it is possible that the decrease in metallicity can also contribute to the small extent of C IV and C III].

Since the metallicity may also vary in a non radially axisymmetric way, because of the complex interplay between near-pristine gas accretion from the IGM, metal-enriched outflows and circulation and mixing in the CGM, we have investigated whether the gas emitting Ly α but not C IV (and not C III]) does show any signature of metal enrichment (i.e. C IV emission) by stacking all spaxels with Ly α but *without* C IV detection together for all objects. For comparison we also stack all the spaxels *with* C IV detection (which always also have Ly α detection). Then we scale two spectra to their Ly α peak flux; this is done to investigate the presence or absence of C IV relative to the Ly α flux, which is a proxy of the content of ionized gas. The two spectra are shown in Figure 9. The former spectrum is labeled by Ly α -C IV, and the latter one is labeled by Ly α +C IV. It is quite clear that C IV is not detected in the Ly α -C IV stack and much weaker (below the detection limit), relative to Ly α , than in the Ly α +C IV stack, despite the S/N of the two stacks being similar. C III] is not detected in both Ly α -C IV and Ly α +C IV stack. This result suggests that the lack of metal lines in the more extended Ly α component of the CGM is likely also associated with a physical lack of metals with respect to the regions de-

tected in CIV. In other words, there might be no much C IV or C III] emission at all outside the area we have already detected with C IV. And this result might hint at a “hard boundary” between the metal rich component and metal poor component of the CGM. At larger radii Ly α is likely to trace a near pristine component of the CGM recently accreted from the IGM and not yet significantly polluted by the metal enriched outflows produced by the quasar.

We finally note that the Ly α -C IV stack shows a broad feature near Ly α , which may be potentially associated with N V. However, this feature appears too broad to be really tracing large scale N V emission associated with the CGM. It is more likely that it is a residual of the strong broad component of the Ly α . As discussed in the previous sections, N V is more difficult to investigate because of both the subtraction of the bright broad component of the quasar nuclear broad Ly α and the continuum discontinuity in this region.

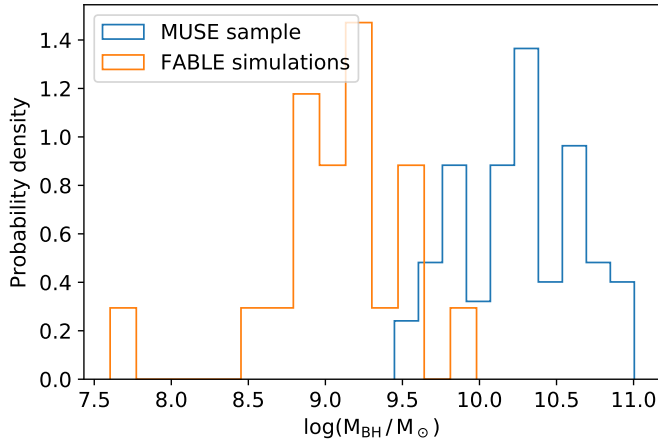


Figure 10. Distribution of the BH masses in the MUSE sample (blue) compared with the distribution of BH masses of the most massive galaxies selected in the FABLE simulation (orange).

4.3. Comparison with Cosmological Simulations

The metal enrichment of galactic haloes as well as the mixing with near-pristine inflows from the IGM is a complex phenomenon which is best investigated through cosmological simulations. In the previous sections we have already discussed some of the results obtained by cosmological simulations (e.g. Hafen et al. 2019; Muratov et al. 2017).

We have investigated the comparison with simulations more quantitatively by exploiting the FABLE simulation suite. The FABLE (Feedback Acting on Baryons in Large-scale Environments) simulations (Henden et al.

2018, 2019a,b, Bennett et al. in prep.) are a suite of state-of-the-art cosmological hydrodynamical simulations of galaxies, groups and clusters performed with the AREPO moving-mesh code (Springel 2010). The simulations employ an updated set of physical models for AGN and supernovae feedback on top of the successful Illustris galaxy formation model (Genel et al. 2014; Vogelsberger et al. 2014; Sijacki et al. 2015) to reproduce the present-day stellar and gas mass fractions of galaxy groups and clusters across a wide halo mass range. For our comparisons we consider the most massive galaxies of the FABLE cluster zoom-in simulations described in Henden et al. (2019a) at $z = 3$, i.e. around the same redshift as the quasars in the MUSE sample. These galaxies are in dark matter halo masses in the range $13.03 < \log(M_{200}/M_\odot) < 13.76$, and have stellar masses in the range $11.01 < \log(M_*/M_\odot) < 11.58$.

Despite selecting the most massive galaxies and despite the size of the FABLE simulation, these galaxies are probably not as massive as the hosts of the very luminous quasars targeted by the MUSE surveys. Although we do not have the masses of the host galaxies of the quasars observed with MUSE, we can compare the black hole masses of the most massive galaxies selected in the FABLE with those measured in the MUSE quasar sample. The BH masses can be considered as a proxy of the galaxy masses, through the $M_{\text{BH}} - \sigma$ relation. As illustrated in Figure 10, the BHs in the MUSE quasar sample (blue histogram) are about an order of magnitude more massive than the quasars in the most massive galaxies selected in the FABLE simulation (orange histogram). Since the metallicity generally scales with mass, it is expected that the FABLE galaxies will be on average less metal rich than the observed sample.

As an example, Figure 11 shows the velocity field, velocity dispersion, gas density and gas metallicity of the CGM in the halo of one of the most massive galaxies in the FABLE simulation at $z = 3$. All quantities are mass-weighted averages. The velocity and velocity dispersion scales are set to match those in Figure 8. The top panels show quantities averaged inside a slice that has a thickness of 5% of the virial radius (on either side of the central galaxy), while in the bottom panels they are averaged across a slice as thick as virial radius. These two cases should bracket what is seen in observations. Indeed, the observations see the gas averaged in projection, however the velocity information allows us to isolate emitting gas clumps along the line-of-sight (although the stacking tends to average out all velocities). Moreover, regions (slices) closer to the quasar are illuminated by a stronger radiation field and therefore tend to emit more strongly and to weight more in the final aver-

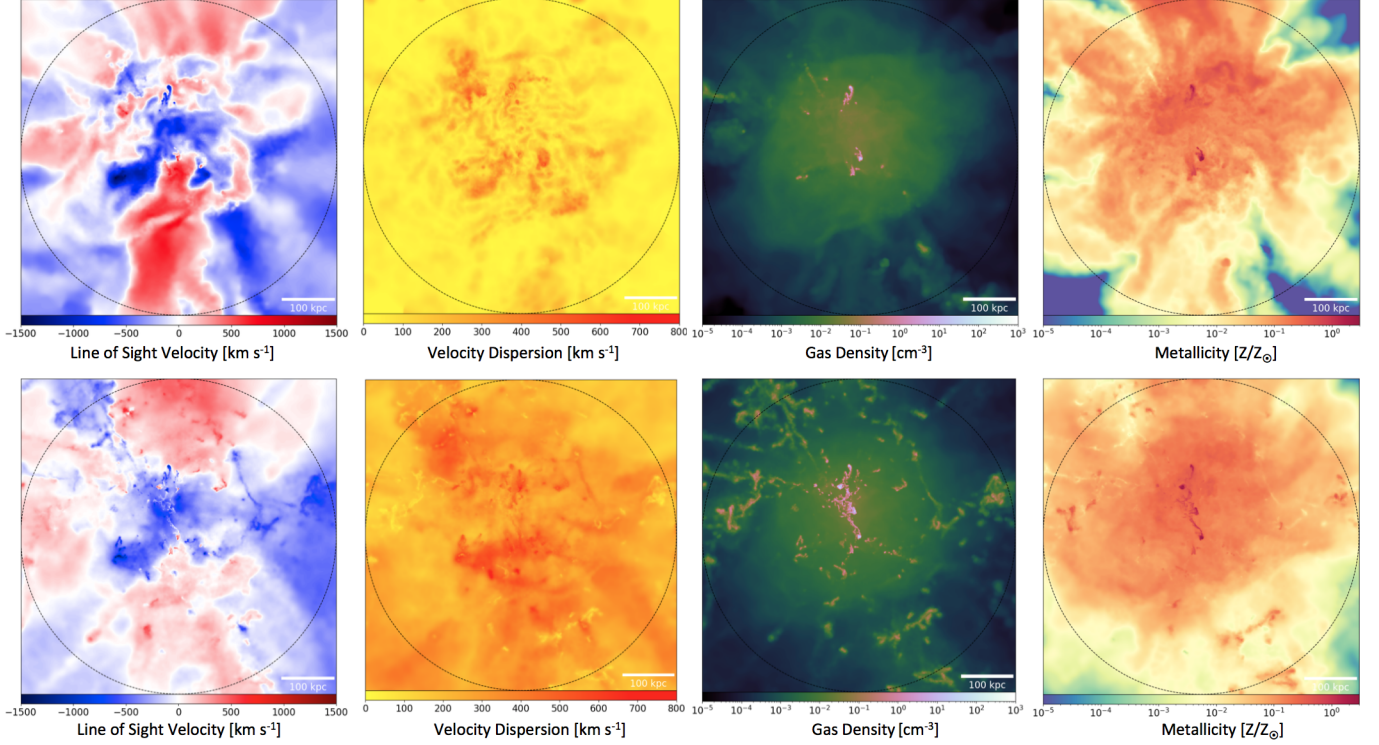


Figure 11. Velocity field, velocity dispersion, gas density and metallicity in the CGM of one of the most massive galaxies at $z = 3$ in the FABLE simulation. All quantities are mass-weighted. The top panels show quantities averaged inside a slice that has a thickness of 5% of the virial radius (on either side of the central galaxy), while in the bottom panels the quantities are averaged across a slice as thick as virial radius. The dashed circle shows the virial radius. The velocity and velocity dispersion scales are set to match those in Figure 8.

aging along the line-of-sight. Finally, the gas emissivity scales as the squared power of the gas density, hence (for a given radiation field) denser clumps dominate the emission of the nebular lines averaged along the line-of-sight. Taking into account all of these observational effects would imply a much more complex treatment of the simulations, which goes beyond the scope of this paper. Here we use the FABLE simulation simply to see whether the main observational features inferred from the MUSE data are generally consistent with the simulations, in a quantitative sense, but we leave a more detailed comparison to a future work.

The simulation clearly shows a complex distribution of both metal poor inflowing streams, metal rich outflows, and more complex patterns. It is interesting to note that similar complex velocity patterns are seen in some of the Ly α velocity fields discussed above for individual objects. The velocity dispersion reaches high values, similar to those inferred from the observations. In the central region, we see enhancement in velocity dispersion similar to Figure 8, which may be a consequence of powerful nuclear outflows. It is also interesting to note that the average gas density is obviously low across most of the CGM, but that there are several clumps around

or even exceeding 10 cm^{-3} ; these are likely dominating the emission that we see in the nebular lines, due to the quadratic dependence of the emissivity on the gas density, and therefore further justifying our choice of the density in the photoionization models. However, within the context of this paper, the main feature to note in the simulation is that there are several regions of the CGM within the virial radius, and even beyond it, that are enriched to metallicities approaching or even exceeding solar, as a result of prominent quasar outflows. At the same time very low metallicity CGM (less than $0.01 Z_{\odot}$ and even down to $10^{-5} Z_{\odot}$) is observed even inside half of the virial radius, close to the galaxy, as a consequence of denser streams from the IGM that manage to pierce into the hot halo.

Clearly, we do not have the sensitivity to map these complex metallicity structures in any of the individual observations in our sample. However, we can compare the radial profiles obtained from our stacks with the radial metallicity profiles likewise extracted from the cosmological simulations. This comparison is illustrated in Figure 12, where the lines show the metallicity profiles of the CGM in various galactic haloes at $z = 3$ in the simulation, color-coded by black hole mass, while the

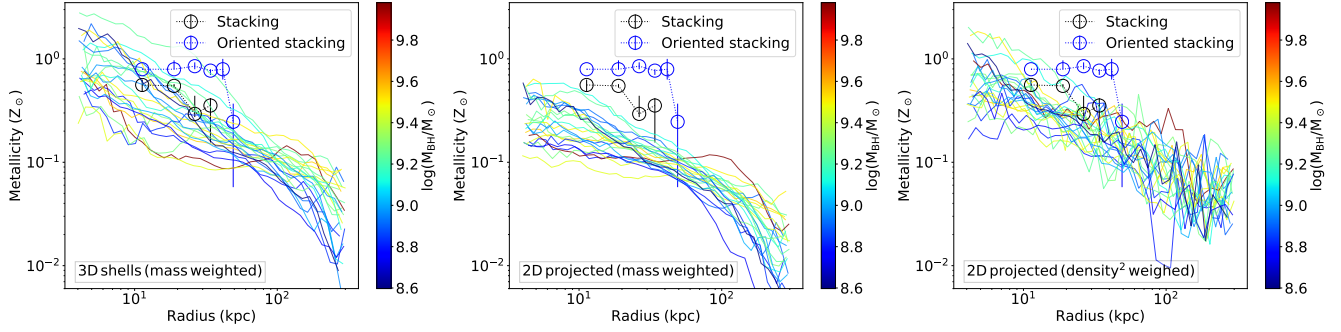


Figure 12. Average radial metallicity profile of the CGM in galactic haloes at $z = 3$ from the FABLE cosmological simulations (lines color-coded by black hole mass) and radial metallicity inferred from the stacked MUSE cubes both for the global stacking (black symbols) and for the stacking of the cubes realigned along the extension of the $\text{Ly}\alpha$ extension (blue symbols). In the leftmost panel the metallicity of the cosmological simulation is averaged inside three-dimensional radial bins and mass-weighted. In the central panels the metallicity is averaged in annuli projected along the line-of-sight and mass-weighted. In the rightmost panel the metallicity is averaged in annuli projected along the line-of-sight and weighted by the square of the gas density (akin to the gas emissivity).

symbols show the metallicity inferred for our stacks at different radial points (black symbols for simple stacks, blue symbols for stacks obtained by re-orienting the cubes along the $\text{Ly}\alpha$ extension) obtained from the grids shown in Figures 5. In the leftmost panel the metallicity of the cosmological simulation is averaged inside three-dimensional radial bins and mass-weighted. In the central panels the metallicity is averaged in annuli projected along the line-of-sight and mass-weighted. In the rightmost panel the metallicity is averaged in annuli projected along the line-of-sight and weighted by the square of the gas density. The latter is expected to be the case closest to the observations, as the emissivity of these nebular lines scales quadratically with density (as long as the densities are lower than the critical densities, which is certainly the case for these transitions in the ISM and CGM), but still not exactly reproducing the case of the observations as this does not yet include the radial geometrical dilution of the quasar ionizing radiation. We have chosen to color-code the simulated haloes by black hole mass as this is supposed to provide a measure of the integrated AGN feedback, hence is expected to possibly scale with the CGM metal enrichment by quasar-driven outflows. However, the metallicity of the simulated massive haloes does not increase monotonically with BH mass; there are haloes with very massive BH and low metallicity, as well as haloes with low mass BH and relatively high metallicity. We do not find any obvious trend even when color-coding the haloes by halo mass (M_{200} , not shown). The lack of clear correlation at this early epoch between metallicity and BH/halo mass reflects the fact that the halo CGM metallicity is strongly dependent on the recent history of accretion from the IGM and the recent enrichment (or lack thereof) by quasar-driven winds. However, one should

also take into account that here we have only selected 20 among the most massive haloes in the simulations and that therefore the dynamic range in terms of halo mass is not large (less than one order of magnitude). A broader range of halo masses should be included to properly investigate the metallicity dependence on halo mass. However, it is interesting to note that the metallicities inferred from the stacked cubes are consistent with the upper envelope of the profiles obtained by the cosmological simulation. The ‘oriented stacking’ profiles are characterized by higher metallicities (though still consistent with the most metal-rich halo in the simulation), not surprisingly, given that in this case we have probably aligned the haloes along the direction of quasar illumination and which is also probably the direction along which metal-loaded outflows are ejected. We also recall that the black holes of these most massive galaxies selected from the simulation are one order of magnitude less massive than those inferred for the quasars observed by MUSE, hence are expected to be less metal enriched than in the observations. More massive simulated systems are expected to result in significantly higher metallicities, even closer to those observed.

Note that the simulations do expect even super-solar metallicities for some haloes in their inner regions, suggesting that also the higher metallicity inferred through the method of Dors et al. (2019) are plausible according to the cosmological simulations.

In the simulation the average radial metallicities drop below $0.1 Z_{\odot}$ at a radial distance larger than about 100 kpc (about half of the virial radius for these massive haloes). As discussed above, and as shown in Figure 11, pockets of low metallicity gas are also likely present well within the central regions of the halo. The presence of such low metallicity gas is observationally confirmed by

the spaxels of $\text{Ly}\alpha$ emitting gas with no CIV, whose stacked spectrum does not show evidence of any metal line (Sect. 4.2 and Figure. 9).

Overall, given the complex physics involved in these physical processes, that are not simple to incorporate in the cosmological simulations, and given the uncertainties affecting the observations, especially for what concerns the nebular lines detections and metallicity measurements, the agreement between our observational results and the expectations from the cosmological simulations is remarkable.

4.4. What Are the Mechanisms Powering the UV Emission Line Nebulae?

Figure 13 shows the luminosity of C IV versus black hole mass (upper panel), total luminosity of quasars (middle panel) and $\text{Ly}\alpha$ luminosity (bottom panel). The total luminosity of quasars is calculated based on a correction factor to the luminosity at 3000\AA (Trakhtenbrot & Netzer 2012). In all three panels, the objects with the detection of C IV are denoted by red circles. Other black symbols provide upper limits. We see no correlation between C IV luminosity and total luminosity, and no correlation between C IV luminosity and black hole mass. This result is not surprising considering the objects in our sample are all at the high mass and high luminosity end of the quasar population (hence limited dynamic range) and also a consequence of the flickering nature of AGNs. However, despite the large number of upper limits and only a limited number of detections, we observe a correlation between C IV luminosity and $\text{Ly}\alpha$ luminosity, as shown in the bottom panel of Figure 13. This suggests, as expected, that the $\text{Ly}\alpha$ and C IV emissions result from photoionization from the same sources, i.e. the quasar radiation field, which is indeed the expectation based on which these very luminous quasars were selected in order to enhance the probability of detecting $\text{Ly}\alpha$ haloes. The correlation between CIV and $\text{Ly}\alpha$ is maintained despite the quasar variability because of the much larger timescales associated with the photoionization of the CGM, involving the light travel time to several tens of kpc in the CGM, which smooths away the AGN variability (e.g. Gilli et al. 2000).

5. SUMMARY AND CONCLUSIONS

Recent MUSE observations have detected extended $\text{Ly}\alpha$ nebulae around quasars at redshift 3–6. In this paper we combine the two samples of quasars observed with MUSE presented in Borisova et al. (2016) and Arigoni Battaia et al. (2019a), the vast majority of which show extended $\text{Ly}\alpha$ nebulae, to make a large MUSE sample of quasars at 3–4. We aim at detecting the

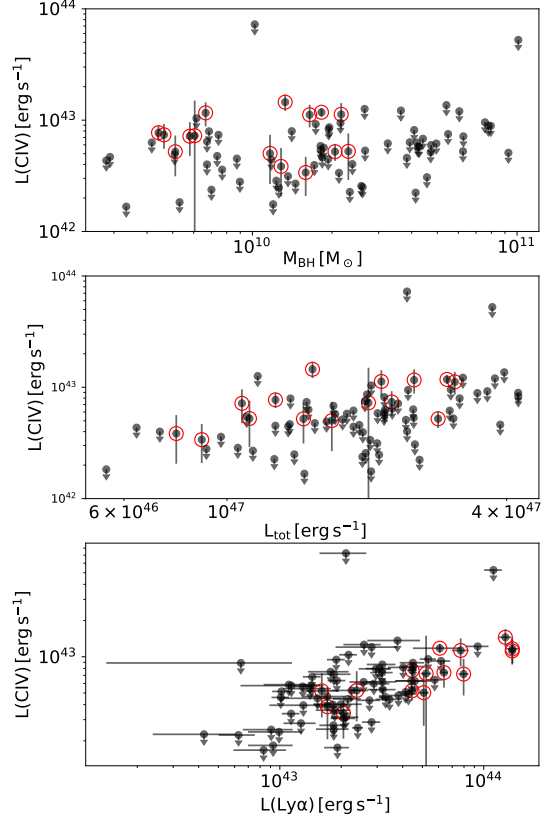


Figure 13. Upper panel: the central black hole mass vs. C IV luminosity. Middle panel: total black hole luminosity vs. C IV luminosity. Bottom panel: the relation between $\text{Ly}\alpha$ luminosity and C IV luminosity. In all three panels, the red circles denote the detections of C IV. All other black dots are upper limits.

diffuse C IV, He II, and C III] emission to constrain the properties of the CGM.

Extended C IV nebulae are found in the haloes of 15 individual quasars. Among these 15 quasars, 4 are radio loud and 11 are radio quiet. 10 objects are detected with extended He II emission, and three of them are radio loud. C III] emission is much fainter and highly contaminated by sky emission in this redshift range. We only detect 4 extended C III] nebulae, with one radio loud object.

Morphologically, the C IV, He II, and C III] nebulae are more compact than the $\text{Ly}\alpha$ nebulae, and are characterized by a range of diverse shapes. The compactness of these nebulae is mostly due to the weakness of these lines, but is likely also associated with a radial drop in ionization conditions and metallicity, as inferred later on with the stacking technique.

The kinematics of the C IV and He II nebulae (no kinematic information could be inferred for the C III] nebulae) are similar to their parent $\text{Ly}\alpha$ nebulae. The

central region is characterized by large velocity dispersion, pointing at quasar-driven outflows, but in the outer regions C IV and He II appear to trace the dynamically more quiescent CGM.

By stacking the cubes of all quasars together (after re-aligning them in redshift and spatially), we obtain average radial profiles of Ly α , C IV, He II, and C III]. We detect these lines out to a radial distance of about 35 kpc from the (stacked) quasar. C IV and He II show a steeper decline with radius than Ly α . The stacked C III] radial profile is shallower than C IV and He II and similar to the radial profile of Ly α . These trends suggest that the decline of C IV and He II is mostly due to a decline in ionization parameter, while the average metallicity changes little with radius at these distances. Indeed, we have used AGN photoionization models to constrain the CGM properties at different distances based on the observed line ratios and we have found that the ionization parameter declines rapidly with radial distance, while the metallicity tend to vary more slowly and is between $0.5 Z_{\odot}$ and Z_{\odot} . We have also stacked the cubes by excluding the few radio-loud quasars and found no significant differences (if anything the metallicity increases slightly).

We have also stacked the quasar cubes by splitting them based on their black hole masses. We have found that haloes hosting more massive black holes are characterized by slightly higher metallicities than haloes hosting less massive black holes. This is not an unexpected trend, given that more massive black holes are hosted in more massive galaxies, which are therefore more metal-rich (based on the mass-metallicity relation), whose outflows are presumably also more metal rich.

For the haloes with strong and very extended Ly α emission we have also stacked the cubes by re-aligning them along the direction of the primary Ly α extension (sometimes referred to as “filaments” by some authors). In this case the signal-to-noise of the stack is significantly enhanced. C IV, He II, and C III] are detected out to a distance of 42 kpc, and we still find that C IV and He II decline more steeply than Ly α , while C III] follows a similar profile as Ly α but scaled down by two orders of magnitude. Also in this case the interpretation with AGN photoionization models give a steeply declining ionization parameter with distance, and a relatively stable metallicity at $0.5 Z_{\odot} < Z < Z_{\odot}$ out to 42 kpc.

The inferred metallicities are somewhat model dependent. We have shown that other recent photoionization models [Dors et al. \(2019\)](#) would give even higher (super-solar) metallicities.

The general idea that Ly α nebulae trace pristine or near-pristine gas recently accreted (or accreting) from

the IGM is challenged by these findings. The high average metallicity ($0.5 Z_{\odot}$ or higher) of Ly α nebulae can not be associated with near-pristine gas accreted from the IGM and must instead be tracing the CGM pre-enriched by galactic outflows. A contribution from gas stripped from satellite galaxies can not be excluded either.

However, by combining all spaxels in the stack that show no evidence for C IV we obtain a high signal-to-noise stacked spectrum that still fails to show any hint of metal lines. Therefore, these components of the Ly α nebulae may actually be associated with very low metallicity gas recently accreted from the IGM.

As a consequence, the Ly α nebulae observed around quasars are characterized by two components: a metal enriched component associated with galactic outflows and a very low metallicity component associated with streams inflowing from the IGM.

We have compared our observational results with the metallicity maps of the CGM of haloes associated with massive galaxies at $z = 3$ in the FABLE cosmological simulations. Such simulated haloes appear indeed characterized by very high metallicities (close to solar or even super-solar) with irregular distribution, but primarily associated with quasar outflows, even out to and beyond the virial radius (i.e. ~ 200 kpc), but also by low metallicity streams entering into the halo down to less than half a virial radius. We have extracted average radial profiles of the metallicity from the simulated massive haloes and find that they show a remarkably good agreement with the average metallicity profile inferred from the stacked MUSE cubes, especially if taking into account that the galaxies in the simulation are one order of magnitude less massive than those observed.

Overall, these results suggest that the observations of Ly α haloes surrounding quasars are capturing the properties of the CGM, associated with metal enrichment by galactic outflows and near-pristine accretion from the IGM, that are expected by the cosmological simulations, even at a quantitative level.

Finally, we investigate the correlation of the C IV luminosity with the quasar properties. There is no clear relation between C IV luminosity and black hole mass, or between C IV luminosity and quasar total luminosity. But there is a positive correlation between C IV luminosity and Ly α luminosity. C IV and Ly α nebulae are likely powered by the same central engine, but due to the flickering and rapidly varying properties of quasars, they are not correlated directly to current properties of central quasars.

Table 1. Quasar Sample and Properties

ID	Quasar	RA (J2000)	Dec (J2000)	Seeing (arcsec)	$z_{Ly\alpha}$ ^a	Exp. T. (min)	$L_{Ly\alpha}$ ^b (10^{43} erg s $^{-1}$)	M_{BH} ^c ($10^{10} M_{\odot}$)	L_{bol} ^d (10^{47} erg s $^{-1}$)	Class ^e
1	SDSS J2319 1040	23:19:34.800	-10:40:36.00	1.4	3.171	42.44	1.53	0.87	1.27	RQ
2	UM 24	00:15:27.400	+06:40:12.00	1.62	3.165	42.29	2.82	6.05	3.77	RQ
3	J 0525 233	05:25:06.500	-23:38:10.00	0.86	3.119	42.88	1.29	1.86	2.18	RL
4	Q 0347 383	03:49:43.700	-38:10:31.00	1.4	3.231	84.71	2.06	4.57	2.54	RQ
5	SDSS J0817 1053	08:17:52.099	+10:53:29.68	1.47	3.332	42.44	3.18	3.25	1.87	RQ
6	SDSS J0947 1421	09:47:34.200	+14:21:17.00	1.21	3.069	42.27	0.64	7.96	3.46	RQ
7	SDSS J1209 1138	12:09:18.000	+11:38:31.00	1.22	3.118	42.23	1.89	2.15	2.45	RQ
8	UM 683	03:36:26.900	-20:19:39.00	1.05	3.132	85.02	4.45	0.44	1.27	RQ
9	Q 0956 1217	09:58:52.200	+12:02:45.00	1.12	3.311	42.25	9.33	3.64	3.22	RQ
10	SDSS J1025 0452	10:25:09.600	+04:52:46.00	1.1	3.242	42.58	7.7	2.17	2.15	RQ
11	Q N1097 1	02:46:34.200	-30:04:55.00	1.18	3.099	42.47	1.71	1.28	0.78	RQ
12	SDSS J1019 0254	10:19:08.255	+02:54:31.94	1.22	3.394	42.1	4.03	4.09	2.18	RQ
13	PKS 1017 109	10:20:10.000	+10:40:02.00	0.91	3.167	242.13	4.45	2.05	2.85	RQ
14	SDSS J2100 0641	21:00:25.030	-06:41:45.00	0.85	3.133	42.49	1.11	1.81	2.11	RQ
15	SDSS J1550 0537	15:50:36.806	+05:37:50.07	1.01	3.145	42.33	5.75	0.67	2.27	RQ
16	SDSS J2348 1041	23:48:56.488	-10:41:31.17	1.72	3.185	42.08	1.44	4.41	1.69	RQ
17	SDSS J0001 0956	00:01:44.886	-09:56:30.83	1.81	3.348	42.24	1.84	2.61	1.4	RQ
18	SDSS J1557 1540	15:57:43.300	+15:40:20.00	0.81	3.291	42.13	12.76	1.33	1.53	RQ
19	SDSS J1307 1230	13:07:10.200	+12:30:21.00	0.89	3.225	42.25	1.84	6.27	2.34	RQ
20	SDSS J1429 0145	14:29:03.033	-01:45:19.00	0.79	3.424	42.4	2.57	4.95	3.02	RQ
21	CT 669	20:34:26.300	-35:37:27.00	0.74	3.219	42.28	6.38	0.46	2.26	RQ
22	Q 2139 4434	21:42:25.900	-44:20:18.00	1.02	3.229	42.32	5.34	7.57	3.03	-
23	Q 2138 4427	21:41:59.500	-44:13:26.00	0.81	3.139	42.12	4.14	9.28	2.43	-
24	SDSS J1342 1702	13:42:33.200	+17:02:46.00	1.03	3.058	43.03	4.41	0.42	1.5	RQ
25	SDSS J1337 0218	13:37:57.900	+02:18:21.00	0.75	3.343	42.39	1.02	4.72	1.77	RQ
26	Q 2204 408	22:07:34.300	-40:36:57.00	0.84	3.185	42.35	11.16	10.11	3.72	-
27	Q 2348 4025	23:51:16.100	-40:08:36.00	0.87	3.331	42.7	3.2	2.67	2.52	-
28	Q 0042 269	00:44:52.300	-26:40:09.00	0.8	3.36	42.49	1.41	1.81	1.1	RQ
29	Q 0115 30	01:17:34.000	-29:46:29.00	0.91	3.227	42.42	1.14	4.27	1.71	RQ
30	SDSS J1427 0029	14:27:55.800	-00:29:51.00	0.95	3.359	42.36	2.17	0.61	2.04	RQ
31	UM 670	01:17:23.300	-08:41:32.00	0.8	3.204	42.63	2.25	6.25	3.07	RQ
32	Q 0058 292	01:01:04.700	-28:58:03.00	1.42	3.1	42.25	2.59	2.66	1.16	RQ
33	Q 0140 306	01:42:54.700	-30:23:45.00	1.39	3.132	42.21	1.61	0.51	1.46	RL
34	Q 0057 3948	00:59:53.200	-39:31:58.00	1.09	3.251	42.27	1.27	0.9	0.9	RQ
35	CTS C22 31	02:04:35.500	-45:59:23.00	1.18	3.247	42.12	2.75	0.28	0.64	-
36	Q 0052 3901A	00:54:45.400	-38:44:15.00	1.25	3.202	42.17	1.71	0.29	1.37	RL
37	UM672	01:34:38.600	-19:32:06.00	1.87	3.128	81.64	0.83	0.33	1.47	RL

Table 1 continued

Table 1 (continued)

ID	Quasar	RA (J2000)	Dec (J2000)	Seeing (arcsec)	$z_{Ly\alpha}$ ^a	Exp. T. (min)	$L_{Ly\alpha}$ ^b (10^{43} erg s ⁻¹)	M_{BH} ^c ($10^{10} M_{\odot}$)	L_{bol} ^d (10^{47} erg s ⁻¹)	Class ^e
38	SDSS J0125 1027	01:25:30.900	-10:27:39.00	0.74	3.351	42.28	1.14	2.12	2.03	RQ
39	SDSS J0100 2105	01:00:27.661	+21:05:41.57	0.73	3.096	42.08	4.27	0.51	1.64	RQ
40	SDSS J0250 0757	02:50:21.800	-07:57:50.00	0.67	3.338	42.46	1.99	2.39	2.44	RQ
41	SDSS J0154 0730	01:54:40.328	-07:30:31.85	0.75	3.335	42.45	2.16	1.93	1.35	RQ
42	SDSS J0219 0215	02:19:38.732	-02:15:40.47	0.64	3.034	42.42	3.82	0.74	1.55	RQ
43	CTSH22 05	01:48:18.130	-53:27:02.00	1.34	3.128	41.96	3.17	0.74	1.48	—
44	SDSS J2321 1558	23:21:54.980	+15:58:34.24	1.61	3.236	42.14	1.43	4.23	1.81	RQ
45	FBQS J2334 0908	23:34:46.400	-09:08:12.24	1.18	3.358	256.69	0.63	4.14	2.6	RL
46	Q2355 0108	23:58:08.540	+01:25:07.20	1.23	3.398	42.19	1.91	3.93	2.52	RQ
47	6dF J0032 0414	00:32:05.380	-04:14:16.21	1.59	3.162	42.18	7.96	0.58	1.08	RL
48	UM 679	02:51:48.060	-18:14:29.00	0.96	3.219	42.21	1.83	1.46	1.14	RQ
49	PKS0537 286	05:39:54.267	-28:39:56.00	0.74	3.138	42.4	2.05	1.59	0.88	RL
50	SDSS J0819 0823	08:19:40.580	+08:23:57.98	0.73	3.205	42.01	13.79	1.65	3.09	RQ
51	SDSS J0814 1950	08:14:53.449	+19:50:18.62	0.75	3.136	42.1	2.38	2.3	1.12	RL
52	SDSS J0827 0300	08:27:21.968	+03:00:54.74	0.96	3.137	41.96	0.91	1.26	2.13	RL
53	SDSS J0905 0410	09:05:49.058	+04:10:10.15	0.93	3.164	42.1	0.93	0.53	0.55	RL
54	S31013 20	10:16:44.319	+20:37:47.29	0.92	3.111	42.04	1.82	0.67	0.72	RL
55	SDSS J1032 1206	10:32:12.886	+12:06:12.83	0.89	3.191	42.15	2.96	0.69	1.37	RL
56	TEX1033 137	10:36:26.886	+13:26:51.75	0.7	3.095	41.98	5.21	0.61	2.02	RL
57	SDSS J1057 0139	10:57:13.250	-01:39:13.79	1.31	3.454	42.02	1.77	5.49	1.98	RL
58	Q1205 30	12:08:12.730	-30:31:07.00	0.63	3.048	42.24	2.11	1.36	2.11	RQ
59	LBQS1244 1129	12:46:40.370	+11:13:02.92	1.45	3.156	42.03	2.89	4.73	2.18	RQ
60	SDSS J1243 0720	12:43:53.960	+07:20:15.47	1.29	3.179	42.01	1.86	0.77	0.97	RL
61	LBQS1209 1524	12:12:32.040	+15:07:25.63	1.42	3.066	42.08	2.11	1.02	2.44	RQ
62	CTS G18 01	00:41:31.4	-49:36:11.9	1.08	3.249	48.32	3.78	5.41	3.95	RQ
63	Q0041 2638	00:43:42.7	-26:22:10.9	1.14	3.076	54.09	0.42	2.33	1.26	RQ
64	Q0042 2627	00:44:33.5	-26:11:25.9	1.18	3.304	48.85	2.82	1.23	1.06	RQ
65	Q0055 269	00:57:58.1	-26:43:15.8	1.02	3.659	551.25	6.09	1.82	2.98	RQ
66	UM669	01:05:16.7	-18:46:41.9	1.31	3.038	54.1	3.45	1.18	1.87	RQ
67	J0124 0044	01:24:04.0	00:44:33.5	0.82	3.841	104.1	4.59	4.19	2.19	RQ
68	UM678	02:51:40.4	-22:00:28.3	0.72	3.208	54.56	0.99	0.7	1.96	RQ
69	CTS B27 07	04:45:33.1	-40:48:42.8	0.59	3.152	49.96	1.92	1.2	2.04	RQ
70	CTS A31 05	05:17:42.1	-37:54:45.9	0.72	3.046	54.72	3.18	1.95	2.0	RQ
71	CT 656	06:00:08.7	-50:40:30.1	0.7	3.154	54.37	1.01	3.84	1.93	RQ
72	AWL 11	06:43:26.9	-50:41:12.9	0.63	3.118	69.04	2.41	2.58	1.99	RQ
73	HE0940 1050	09:42:53.6	-11:04:26.0	0.74	3.091	48.93	4.49	7.8	4.23	RQ
74	BR1108 07	11:11:13.7	-08:04:03.0	0.98	3.935	104.29	5.08	1.17	1.68	RQ
75	CTS R07 04	11:13:50.1	-15:33:40.2	0.94	3.366	48.7	13.82	0.67	2.53	RQ
76	Q1317 0507	13:20:29.8	-05:23:34.2	0.94	3.719	421.51	6.18	1.74	3.63	RQ

Table 1 continued

Table 1 (*continued*)

ID	Quasar	RA (J2000)	Dec (J2000)	Seeing (arcsec)	$z_{Ly\alpha}$ ^a	Exp. T. (min)	$L_{Ly\alpha}$ ^b (10^{43} erg s ⁻¹)	M_{BH} ^c ($10^{10} M_{\odot}$)	L_{bol} ^d (10^{47} erg s ⁻¹)	Class ^e
77	Q1621 0042	16:21:16.7	-00:42:48.2	0.85	3.707	198.46	3.07	1.41	3.17	RQ
78	CTS A11 09	22:53:10.7	-36:58:15.9	0.76	3.147	54.49	1.3	1.71	1.96	RQ
79	PKS1937 101	19:39:57.4	-10:02:39.9	0.75	3.791	155.68	4.51	1.94	4.24	RL
80	QB2000 330	20:03:24.1	-32:51:45.9	0.96	3.789	528.28	3.3	1.84	3.88	RL

^a $Ly\alpha$ redshift measured from diffuse $Ly\alpha$ nebulae.

^b $Ly\alpha$ luminosity measured from the PSF subtracted datacubes with circular aperture photometry with a radius of 3 arcsec.

^c Black hole mass computed from quasar continuum luminosity at 1450Å and FWHM of C IV, following the method of Trakhtenbrot & Netzer (2012).

^d Quasar bolometric luminosity corrected by continuum luminosity at 3000Å based on the method of Trakhtenbrot & Netzer (2012).

^e RQ: radio quiet quasar; RL: radio loud quasar; the 6 sources labeled by – are not covered by any radio survey.

We acknowledge support from the National Science Foundation of China (11721303, 11890693) and the National Key R&D Program of China (2016YFA0400703).

RM acknowledges ERC Advanced Grant 695671 “QUENCH” and support by the Science and Technology Facilities Council (STFC).

APPENDIX

A. PSEUDO-NB IMAGES FOR ALL OBJECTS

In this section, we show the pseudo-NB images for all objects. In Figure A.1, we show the atlas of the detected Ly α nebulae for the 80 quasars. These systems have very different shapes and sizes. Several of the Ly α nebulae are symmetric with physical scales smaller than 50 kpc. Several very extended objects (e.g., No. 13, 47, 50, 65, etc.) show very asymmetric emission. We compare these nebulae with those from Borisova et al. (2016) and Arrigoni Battaia et al. (2019a), and find that they broadly agree with each other.

Out of 80 quasars, 15 are detected with extended C IV emission, as shown in Figure A.2. These C IV nebulae are more compact than their Ly α counterparts. Ten objects are detected with extended He II emission, as shown in Figure A.3. Three objects are radio loud, and the others are radio quiet. The He II morphology is generally similar to that of C IV. Only 4 objects are detected with extended C III] emission, with 1 radio loud object, as shown in Figure A.4. For objects at redshift 3~4, the C III] line highly contaminated by OH sky lines.

REFERENCES

- Anderson, M. E., Churazov, E., & Bregman, J. N. 2016, *MNRAS*, 455, 227
- Arrigoni Battaia, F., Hennawi, J. F., Prochaska, J. X., et al. 2019a, *MNRAS*, 482, 3162
- Arrigoni Battaia, F., Prochaska, J. X., Hennawi, J. F., et al. 2018, *MNRAS*, 473, 3907
- Arrigoni Battaia, F., Obreja, A., Prochaska, J. X., et al. 2019b, arXiv e-prints, arXiv:1909.00829
- Bacon, R., Accardo, M., Adjali, L., et al. 2010, in *Society of Photo-Optical Instrumentation Engineers (SPIE) Conference Series*, Vol. 7735, Proc. SPIE, 773508
- Bischetti, M., Piconcelli, E., Feruglio, C., et al. 2019, *A&A*, 628, A118
- Borisova, E., Cantalupo, S., Lilly, S. J., et al. 2016, *ApJ*, 831, 39
- Bowen, D. V., Chelouche, D., Jenkins, E. B., et al. 2016, *ApJ*, 826, 50
- Cai, Z., Fan, X., Yang, Y., et al. 2017, *ApJ*, 837, 71
- Cai, Z., Hamden, E., Matuszewski, M., et al. 2018, *ApJL*, 861, L3
- Cano-Díaz, M., Maiolino, R., Marconi, A., et al. 2012, *A&A*, 537, L8
- Cantalupo, S., Arrigoni-Battaia, F., Prochaska, J. X., Hennawi, J. F., & Madau, P. 2014, *Nature*, 506, 63
- Carniani, S., Marconi, A., Maiolino, R., et al. 2015, *A&A*, 580, A102
- . 2017, *A&A*, 605, A105
- Chen, H.-W., Johnson, S. D., Straka, L. A., et al. 2019, *MNRAS*, 484, 431
- Chisholm, J., Tremonti, C., & Leitherer, C. 2018, *MNRAS*, 481, 1690
- Cicone, C., Maiolino, R., Sturm, E., et al. 2014, *A&A*, 562, A21
- Cicone, C., Maiolino, R., Gallerani, S., et al. 2015, *A&A*, 574, A14
- Crain, R. A., McCarthy, I. G., Schaye, J., Theuns, T., & Frenk, C. S. 2013, *MNRAS*, 432, 3005
- Dors, O. L., J., Arellano-Córdova, K. Z., Cardaci, M. V., & Hägele, G. F. 2017, *MNRAS*, 468, L113
- Dors, O. L., Agarwal, B., Hägele, G. F., et al. 2018, *MNRAS*, 479, 2294
- Dors, O. L., Cardaci, M. V., Hägele, G. F., & Krabbe, A. C. 2014, *MNRAS*, 443, 1291
- Dors, O. L., Monteiro, A. F., Cardaci, M. V., Hägele, G. F., & Krabbe, A. C. 2019, *MNRAS*, 486, 5853
- Drake, A. B., Farina, E. P., Neeleman, M., et al. 2019, arXiv e-prints, arXiv:1906.07197
- Farina, E. P., Venemans, B. P., Decarli, R., et al. 2017, *ApJ*, 848, 78
- Fluetsch, A., Maiolino, R., Carniani, S., et al. 2019, *MNRAS*, 483, 4586
- Genel, S., Vogelsberger, M., Springel, V., et al. 2014, *MNRAS*, 445, 175
- Gilli, R., Maiolino, R., Marconi, A., et al. 2000, *A&A*, 355, 485
- Ginolfi, M., Maiolino, R., Carniani, S., et al. 2018, *MNRAS*, 476, 2421
- Gutkin, J., Charlot, S., & Bruzual, G. 2016, *MNRAS*, 462, 1757
- Hafen, Z., Faucher-Giguère, C.-A., Anglés-Alcázar, D., et al. 2019, *MNRAS*, 488, 1248

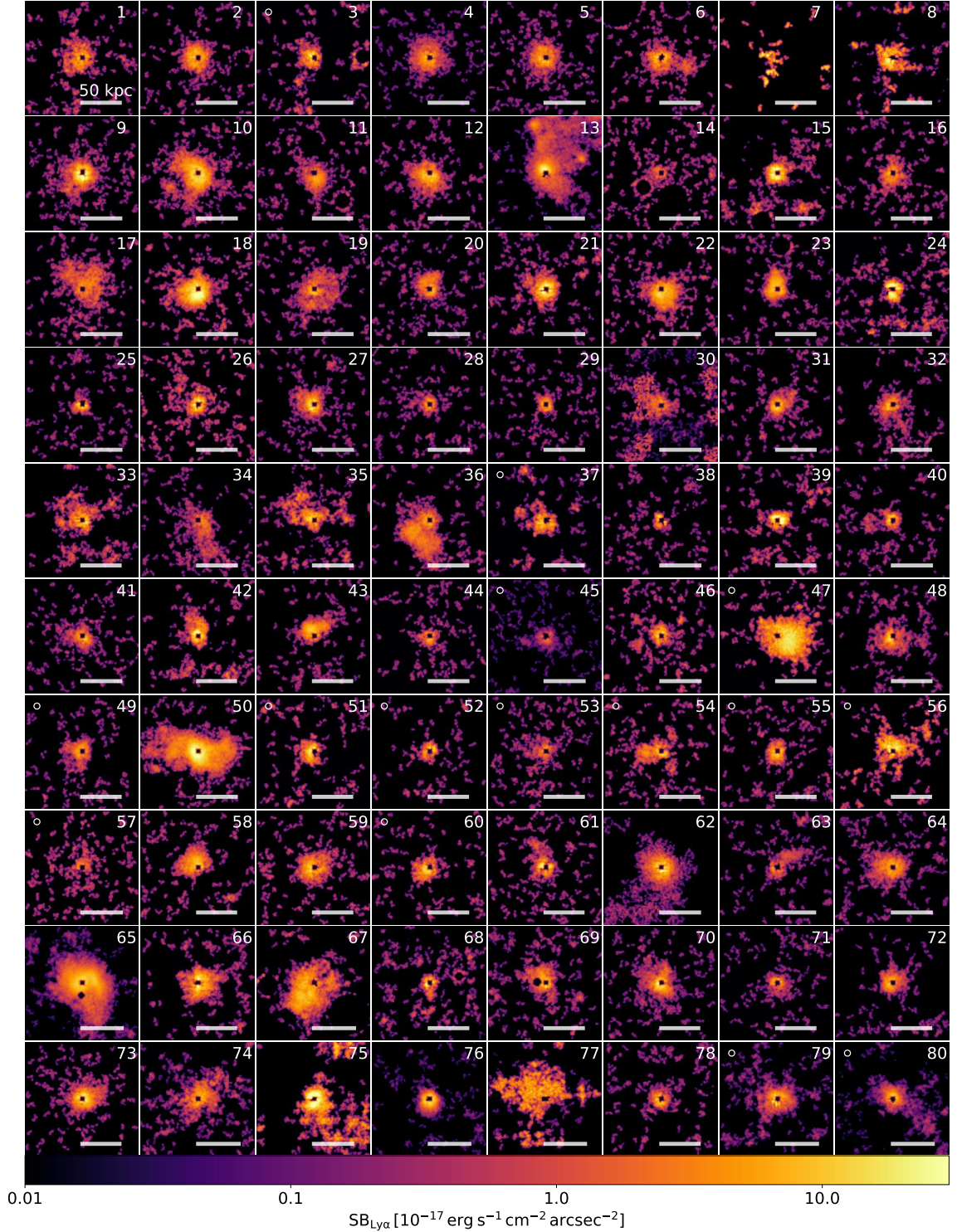


Figure A.1. Pseudo-NB images of the Ly α emission around quasars. In each panel, the original position of each quasar is masked by a small ($1'' \times 1''$) black square. Each thumbnail has a size of $20'' \times 20''$, corresponding to about 150 kpc at the median redshift of the sample.

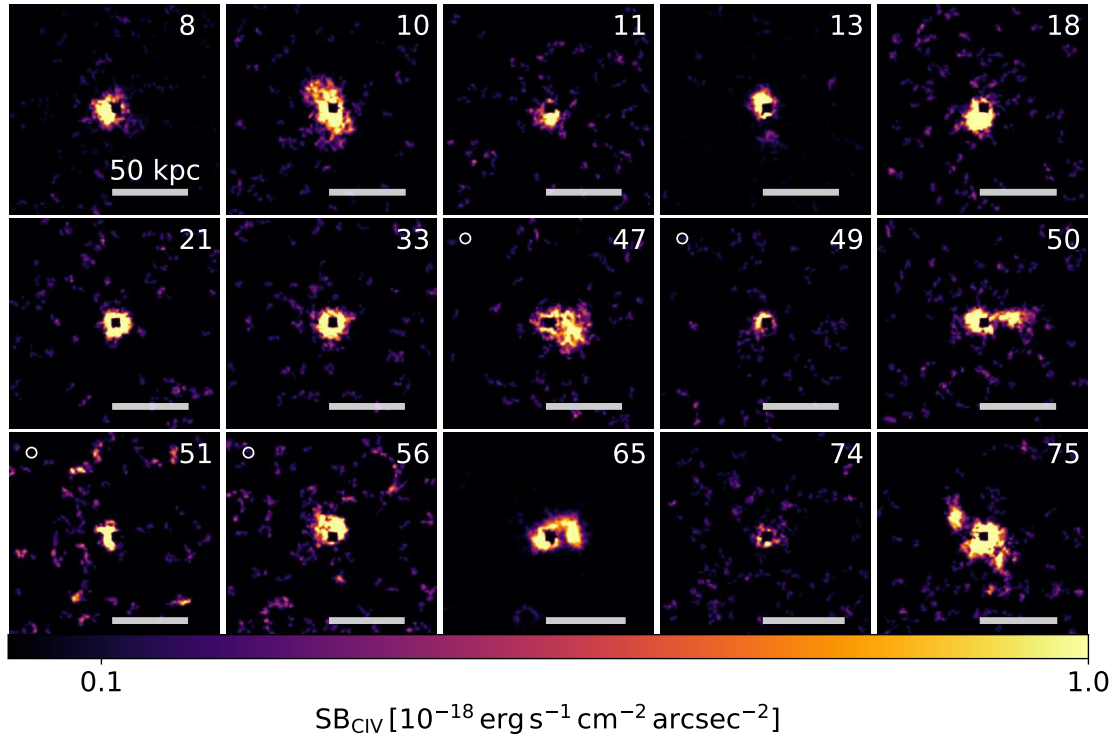


Figure A.2. The same as Figure A.1, but for C IV.

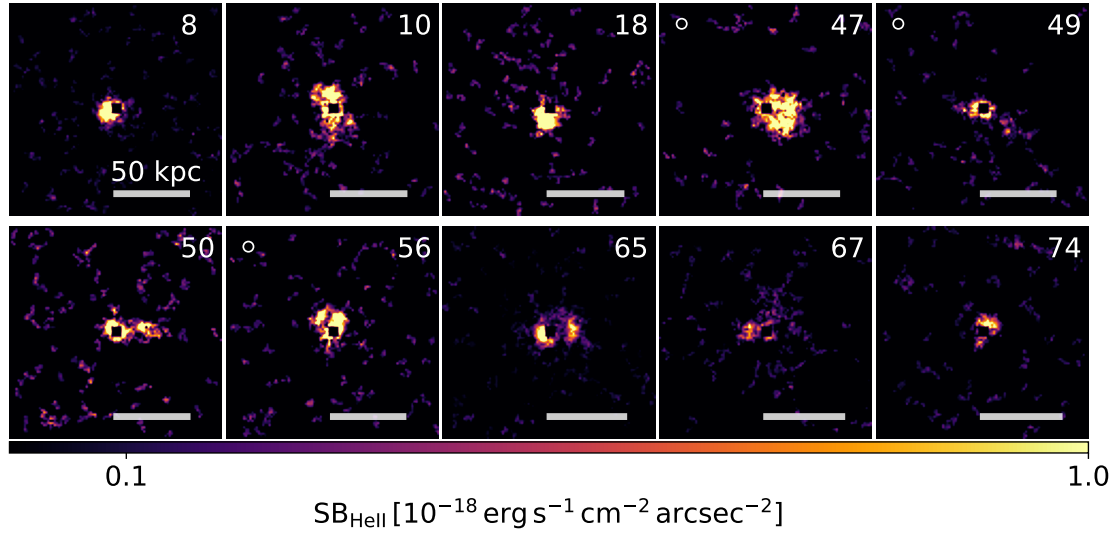


Figure A.3. The same as Figure A.1, but for He II.

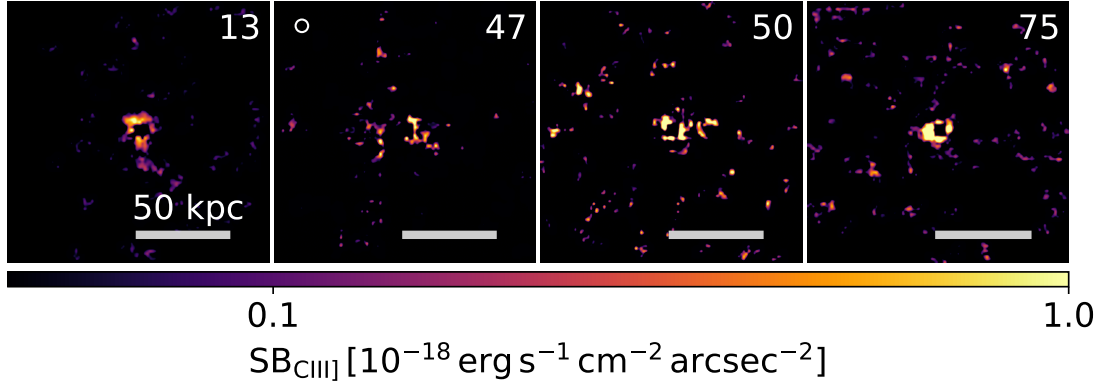


Figure A.4. The same as Figure A.1, but for C III].

- Henden, N. A., Puchwein, E., Shen, S., & Sijacki, D. 2018, *MNRAS*, 479, 5385
- Henden, N. A., Puchwein, E., & Sijacki, D. 2019a, *MNRAS*, 2230
- . 2019b, arXiv e-prints, arXiv:1911.12367
- Humphrey, P. J., Buote, D. A., Canizares, C. R., Fabian, A. C., & Miller, J. M. 2011, *ApJ*, 729, 53
- Lehner, N., Howk, J. C., & Wakker, B. P. 2015, *ApJ*, 804, 79
- Lusso, E., Fumagalli, M., Fossati, M., et al. 2019, *MNRAS*, 485, L62
- Maiolino, R., & Mannucci, F. 2019, *A&A Rv*, 27, 3
- Maiolino, R., Nagao, T., Grazian, A., et al. 2008, in *Astronomical Society of the Pacific Conference Series*, Vol. 396, *Formation and Evolution of Galaxy Disks*, ed. J. G. Funes & E. M. Corsini, 409
- Maiolino, R., Gallerani, S., Neri, R., et al. 2012, *MNRAS*, 425, L66
- Martin, C. L., Ho, S. H., Kacprzak, G. G., & Churchill, C. W. 2019, *ApJ*, 878, 84
- Maseda, M. V., Brinchmann, J., Franx, M., et al. 2017, *A&A*, 608, A4
- Matejek, M. S., & Simcoe, R. A. 2012, *ApJ*, 761, 112
- Matsuda, Y., Yamada, T., Hayashino, T., et al. 2011, *MNRAS*, 410, L13
- Matsuoka, K., Nagao, T., Maiolino, R., Marconi, A., & Taniguchi, Y. 2009, *A&A*, 503, 721
- Matsuoka, K., Nagao, T., Marconi, A., et al. 2018, *A&A*, 616, L4
- Matsuoka, K., Nagao, T., Marconi, A., Maiolino, R., & Taniguchi, Y. 2011, *A&A*, 527, A100
- McIntosh, D. H., Rieke, M. J., Rix, H. W., Foltz, C. B., & Weymann, R. J. 1999, *ApJ*, 514, 40
- Mignoli, M., Feltre, A., Bongiorno, A., et al. 2019, *A&A*, 626, A9
- Mingozi, M., Cresci, G., Venturi, G., et al. 2019, *A&A*, 622, A146
- Muratov, A. L., Kereš, D., Faucher-Giguère, C.-A., et al. 2017, *MNRAS*, 468, 4170
- Nagao, T., Maiolino, R., & Marconi, A. 2006, *A&A*, 447, 863
- Nakajima, K., Schaerer, D., Le Fèvre, O., et al. 2018, *A&A*, 612, A94
- Nelson, D., Kauffmann, G., Pillepich, A., et al. 2018, *MNRAS*, 477, 450
- Onodera, M., Carollo, C. M., Lilly, S., et al. 2016, *ApJ*, 822, 42
- Peeples, M. S., Werk, J. K., Tumlinson, J., et al. 2014, *ApJ*, 786, 54
- Pérez-Montero, E., & Amorín, R. 2017, *MNRAS*, 467, 1287
- Putman, M. E., Peek, J. E. G., & Joun, M. R. 2012, *ARA&A*, 50, 491
- Rauch, M., & Haehnelt, M. G. 2011, *MNRAS*, 412, L55
- Revalski, M., Crenshaw, D. M., Kraemer, S. B., et al. 2018, *ApJ*, 856, 46
- Rubin, K. H. R., Hennawi, J. F., Prochaska, J. X., et al. 2015, *ApJ*, 808, 38
- Schirmer, M., Diaz, R., Holm, K., Levenson, N. A., & Winge, C. 2013, *ApJ*, 763, 60
- Shen, Y., Brandt, W. N., Richards, G. T., et al. 2016, *ApJ*, 831, 7
- Sijacki, D., Vogelsberger, M., Genel, S., et al. 2015, *MNRAS*, 452, 575
- Springel, V. 2010, *MNRAS*, 401, 791
- Trakhtenbrot, B., & Netzer, H. 2012, *MNRAS*, 427, 3081
- Tremonti, C. A., Heckman, T. M., Kauffmann, G., et al. 2004, *ApJ*, 613, 898
- Tripp, T. M., Meiring, J. D., Prochaska, J. X., et al. 2011, *Science*, 334, 952
- Troncoso, P., Maiolino, R., Sommariva, V., et al. 2014, *A&A*, 563, A58

- Tumlinson, J., Peeples, M. S., & Werk, J. K. 2017, *ARA&A*, 55, 389
- Turner, M. L., Schaye, J., Steidel, C. C., Rudie, G. C., & Strom, A. L. 2014, *MNRAS*, 445, 794
- Vangioni, E., Dvorkin, I., Olive, K. A., et al. 2018, *MNRAS*, 477, 56
- Venemans, B. P., Walter, F., Decarli, R., et al. 2017, *ApJ*, 845, 154
- Villar-Martín, M., Sánchez, S. F., Humphrey, A., et al. 2007, *MNRAS*, 378, 416
- Vogelsberger, M., Genel, S., Springel, V., et al. 2014, *MNRAS*, 444, 1518
- Witstok, J., Puchwein, E., Kulkarni, G., Smit, R., & Haehnelt, M. G. 2019, arXiv e-prints, arXiv:1905.06954
- Xu, F., Bian, F., Shen, Y., et al. 2018, *MNRAS*, 480, 345
- Yuma, S., Ouchi, M., Drake, A. B., et al. 2017, *ApJ*, 841, 93
- Yuma, S., Ouchi, M., Fujimoto, S., Kojima, T., & Sugahara, Y. 2019, arXiv e-prints, arXiv:1904.11510